The Detection and Triggering of Forward Muons using the H1 Detector

Kirstee Louise Hewitt

Thesis submitted for the degree of
Master of Philosophy

School of Physics and Space Research
Faculty of Science
University of Birmingham

March 1996

This work was supported financially by the University of Birmingham.

Abstract

The electron-proton colliding beam facility consists of two independent accelerators designed to store 820 GeV protons and 30 GeV electrons. The two beams circulate in opposite directions in an underground tunnel, 6.3 km in length. At two interaction points the beams are directed against each other and some of the highest collision energies ever attained are observed. The H1 detector is situated at one of these interaction points and observes the reaction products from these collisions.

This report firstly discusses briefly the physics potential that HERA has to offer and follows this by a description of the H1 detector at HERA. Particular emphasis is laid on the subdetectors which can be found in the 'forward direction' (the direction of the proton beam) which is defined by the angular region $3° < \theta < 20°$. My studies have concentrated on the detection and triggering of muons within this region.

Muons are detected in the forward region by the Forward Tracking Detector (FTD), the instrumented iron (which surrounds the whole of the H1 experiment), and the Forward Muon Detector (FMD). I have studied the correlation of muon momenta measured in the FTD and the FMD and find significant differences which are attributed to problems with the FTD. Additionally, I have made a preliminary determination of the efficiency and acceptance of the Forward Muon Trigger. These are both important steps toward analysing forward muon producing processes.

Contents

List of Figures

List of Tables

Chapter 1

Introduction

Particle physics is the study of the fundamental constituents of matter and their interactions. A modern theory called the Standard Model has resulted from the interpretation of experimental data in terms of the basic properties of a set of fundamental particles.

1.1 The Standard Model

The formulation of the Standard Model of particle physics seems to provide, at least in principle, a basis for all known physical phenomena except gravity. The properties and interactions of a small number of particles of three distinct types underlie the model. The first two types are spin-$\frac{1}{2}$ fermions and are called *quarks* and *leptons*; the third type is a set of spin-1 bosons called *gauge bosons* which act as the 'force carriers' within the framework of Gauge Field Theories. All experimental evidence is consistent with the idea that these particles are point like which means they have no internal structure or excited states.

There are six distinct types or flavours of quarks and leptons. They occur in three pairs or generations as illustrated in table 1.1.

There are six known leptons, and associated with the three charged leptons there are three neutral leptons (neutrinos) which are assumed to have zero mass within the Standard Model. The charged leptons interact via the *electromagnetic* force, the

	CHARGE	GENERATIONS I	II	III
QUARKS	+2/3	up	charm	top
	-1/3)	down	strange	bottom
LEPTONS	-1	e	μ	τ
	0	ν_e	ν_μ	ν_τ

Table 1.1: The three generations of fermions within the Standard Model.

weak force and the *gravitational* force. At present the neutrinos have only been seen to interact via the weak force.

The quark generations consist of a quark of charge $+\frac{2}{3}$ (u,c, or t) together with a quark of charge -$\frac{1}{3}$ (d,s, or b) in units of e. They are called *down* (d), *up* (u), *strange* (s), *charm* (c), *bottom* (b) and *top* (t) quarks. There is strong experimental evidence that the first five flavours exist but the existence of the sixth quark, t, is still under investigation. It is believed to have been observed by the CDF [1] and D0 [2] collaborations at the Fermilab Tevatron accelerator (proton - antiproton collider).

The quarks and their bound states, namely hadrons (three quarks or anti-quarks form baryons; a quark and anti-quark pair form mesons), interact via an additional force known as the *strong* force. They also interact via the gravitational, the weak and the electromagnetic forces, although these forces have a small coupling strength compared to the strong force.

1.1.1 The Four Fundamental Forces of Nature

Three of the fundamental forces of nature, the *electromagnetic*, the *weak* and the *strong* forces have already been mentioned in context with the three generations of fermions. In addition to these there is a fourth force known as *gravity.* The gravitational interaction between elementary particles is so small compared to the other three that reference here will only be made to the 'three forces of nature'.

The Electromagnetic Interaction

Electromagnetism is described to the limit of experimental accuracy by a quantum field theory known as Quantum Electrodynamics or QED. QED is formulated within the framework of Lagrangian field theory. The Lagrangian is defined by:

$$L = T - V$$

where T and V are the kinetic and potential energies of the system respectively. The Lagrangian of QED is unchanged under arbitrary phase transformations of the electron field, $\psi(x)$, and corresponding changes in the photon field, $A_\mu(x)$, that depend on the position x in space time. Hence, QED is a 'local gauge' theory as oppose to a 'global gauge' theory in which a constant phase transformation is applied to $\psi(x)$ and $A_\mu(x)$ at all space time points.

$\psi(x)$ may be altered by an arbitrary phase factor provided that $A_\mu(x)$ is simultaneously adjusted in a suitable way. The photon field plays an intrinsic part and there could be no local gauge invariance without it. Therefore, if the postulate of this local gauge invariance is taken for spin$-\frac{1}{2}$ particles, the existence of gauge bosons (in this case photons) is required and also their coupling to fermions must be specified. Local gauge invariance also requires that the gauge bosons (photon) be massless.

The Strong Force

The theory describing the strong interactions experienced by hadrons is known as Quantum Chromodynamics or QCD. QCD is similar to QED in that both describe interactions which are mediated by massless spin-1 bosons. In the case of QCD, the bosons form an octet of massless and chargeless particles (like photons) called gluons. However, instead of coupling to the electric charge, they couple to the colour charges of the quarks.

Colour charge was predicted from the result of finding that for baryons the combined space, spin and flavour wavefunctions of their component quarks are symmetric (e.g. the Δ^{++} baryon which consists of three 'u' quarks with spins aligned in an S state of relative motion). The Pauli Principle predicts that the wavefunction of any state must be antisymmetric under the interchange of any two identical spin-$\frac{1}{2}$ fermions. As a result, the colour degree of freedom was introduced which restored the overall antisymmetry of the total wavefunction because the quark colour wavefunction is antisymmetric.

The coupling strength of QCD (α_s), corresponding to the fine structure constant of electromagnetism, is predicted to vary logarithmically with the four momentum transfer (Q^2) of the interaction. At low Q^2, α_s is large and the force is strong leading to the binding of quarks in hadrons. At high Q^2, as at HERA, the value of α_s becomes much smaller than unity and the quark structure of the proton can be probed.

The Weak Interaction

This force is also associated with the exchange of spin-1 particles but, in contrast to photons and gluons, these bosons are very massive and the resulting interactions are consequently of very short range. There are three such 'intermediate vector bosons' namely the charged W^+ and W^- and the neutral Z°.

In the 1960's Glashow, Salam and Weinberg developed a theory which unified the electromagnetic and weak interaction that correctly predicted the existence of these bosons which were observed subsequently at CERN in 1983. The theory is fully consistent with all the data on both weak and electromagnetic interactions (referred to collectively as the *electroweak* interaction - analogous to the *electromagnetic* interaction). The new unification in which the weak and electromagnetic forces acquire equal strength is manifest at high energies compared to the boson masses. At lower energies the interactions can quite clearly be separated having very different strengths. The weak interaction is responsible for the phenomena of β decay.

1.2 Physics at HERA

HERA is the first ever ep collider. It accelerates and stores 820 GeV protons and 30 GeV electrons (or positrons), which when collided will give an approximate center of mass energy of 314 GeV. Compared to previous fixed target experiments, HERA provides an increase in spatial resolving power of one order of magnitude. The corresponding four momentum transfer squared (q^2 or $-Q^2$) can reach $4 \times 10^4\ \mathrm{GeV}^2$, which is at least two orders of magnitude larger than ever before.

The proton is made up from point-like constituents and the evidence for this comes from deep inelastic lepton-proton scattering (see section 1.2.1). The momentum fraction of the total proton momentum is measured by the Bjorken x variable that is defined by equation 1.2. Structure functions are defined which quantify the distribution of x for the partons (quarks and gluons). These structure functions can be measured at HERA in the kinematic region of very small x. There is also potential to study the weak charged current at high momentum transfer; measurement of the momentum distributions for heavy quarks and other heavy flavour physics; photoproduction; and possible production of exotic particles such as leptoquarks.

1.2.1 Lepton-Proton Scattering at HERA

In the kinematic range at HERA the electron(positron)-proton scattering is mainly dominated by the neutral current (NC) scattering process :

$$l(k) + p(P) \longrightarrow l(k') + H$$

where H represents the final hadronic state. The four momentum transfer squared, Q^2, is defined as

$$Q^2 \equiv -q^2 = -(k - k')^2 \tag{1.1}$$

where q is the four momentum of the virtual exchange particle. The reaction is mediated either by a virtual photon or Z° boson. For charged current interactions, in which the $W^\pm$ boson is exchanged, the interaction is of the general form

$$l + p \longrightarrow \nu_l + H.$$

Interactions involving the exchange of a Z° or $W^\pm$ only occur for high values of Q^2 . The region of $Q^2 > \mathcal{O}(4\,\mathrm{GeV}^2)$, accessible to electron detection using the main H1 calorimeter and for which α_s is becoming small, is generally regarded as 'Deep Inelastic Scattering' (DIS). However, interactions in which the momentum transfer is small, i.e. $Q^2 < \mathcal{O}(1\,\mathrm{GeV}^2)$, and are mediated by the exchange of a quasi-real photon are referred to as 'photoproduction' interactions.

1.2.2 Deep-Inelastic Scattering

In a typical DIS event, where the scattered lepton is detected in the calorimeter, its measured three momentum can be used to determine the event kinematics.The measured quantities are therefore the initial and final state lepton energies, E_l and $E_{l'}$, and the lepton scattering angle, θ. However, it is more convenient to work with the Lorentz invariant Bjoken scaling variables Q^2 and x. The definition for Q^2 has already been given and x is defined as

$$x \equiv Q^2/(2P.q). \tag{1.2}$$

Further useful variables are :

$$y \equiv (P.q)/(P.k) \tag{1.3}$$

and

$$W^2 \equiv (q+P)^2 \simeq Q^2(1-x)/x \tag{1.4}$$

where W is the total hadronic invariant mass and also the photoproduction center of mass energy. In figure 1.1 the mechanism of a DIS ep interaction is shown.

The variables x and y are visualised easily in a reference frame in which the target proton has a very large momentum e.g. the center of mass frame at HERA. In such a frame, the momenta of the constituents will be almost collinear with the proton momentum, so that to a good approximation the target can be viewed as a stream of partons each carrying a fraction of the proton momentum, P. For $Q^2 \gg M^2$ (where M is the mass of the proton), the fraction of the proton momentum carried by the struck quark is given by x [3, 4]. The variable y can be interpreted as the

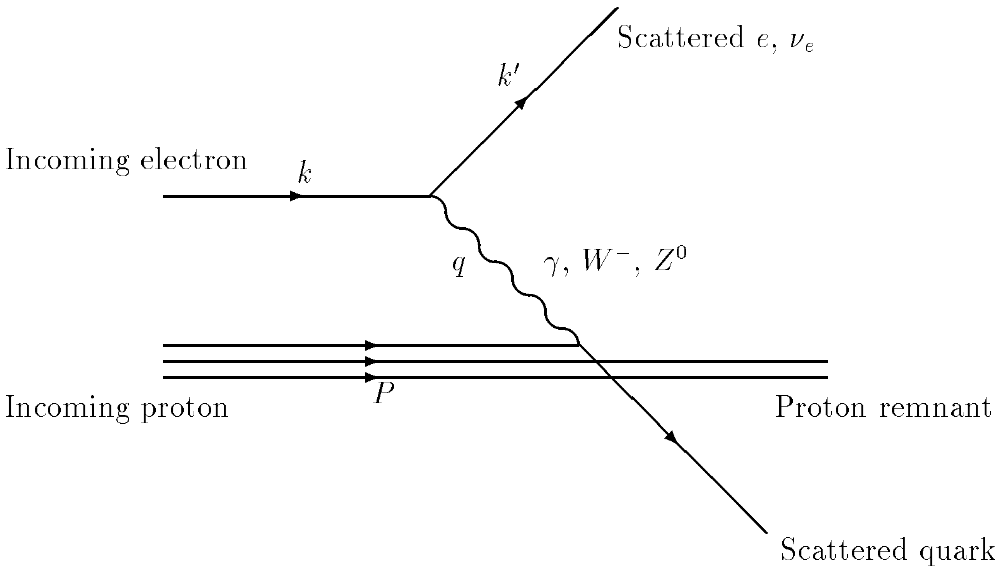

Figure 1.1: A schematic representation of DIS.

fraction of energy that the incident lepton transfers to the proton measured in the rest frame of the incident proton.

The variables Q^2, x and y are related by the equation

$$Q^2 = sxy \tag{1.5}$$

where s is the center of mass energy squared and is defined by

$$s \equiv (k+P)^2 \simeq 4E_eE_p \tag{1.6}$$

where E_e is the electron beam energy and E_p the proton beam energy.

It can also be shown that the variables y and Q^2 can be expressed in terms of the final state scattering angle, θ, and the final state energy, $E_{e'}$, of the scattered lepton by

$$Q^2 = 4E_eE_{e'}\cos^2\left(\frac{\theta}{2}\right) \tag{1.7}$$

and

$$y = 1 - \frac{E_{e'}}{E_e}\sin^2\left(\frac{\theta}{2}\right). \tag{1.8}$$

1.2.3 Photoproduction

The total cross section for events at HERA is primarily due to photoproduction (γp) events because the flux of virtual photons from the electron peaks at $Q^2 = 0$. Such events open up a wide spectrum of QCD studies ranging from perturbative to non-perturbative physics. Since photoproduction events have such a high rate, they may contribute a major background to other physics processes. Early physics analysis of the HERA data was heavily focused on such events.

Photoproduction events are mediated by a quasi-real photon with a $Q^2 \approx 0$. The electron is scattered at small angles and may be detected in the electron tagger detector which is positioned downstream in the electron direction. A non-perturbative description of such processes provided by the vector-dominance-meson model (VDM) [6, 7] , where the incident photon fluctuates into a virtual vector meson which interacts through the strong force with the proton. This is considered to be a 'soft' photoproduction process. There also exist photoproduction processes which are known as 'hard' processes. These involve the photon interacting with the constituents of the proton in a point-like manner. Hard photoproduction interactions may be split up into *direct* and *resolved* processes.The interactions classed as direct are those such as photon-gluon fusion and QCD Compton Scattering. Resolved processes, however, involve the photon being resolved into partons before one such component interacts with the proton.

The total cross-section for photoproduction can be thought of as the total cross-section for nearly real photons. In the region of low Q^2, the incident electron beam can be considered as a source of photons with a flux given by the Weizsacker-Williams approximation [8]. Using this approximation the cross-section for low Q^2 ep-scattering events can be related to the total photoproduction cross-section by

$$\frac{d^2\sigma_{ep}}{dxdy} = \frac{\alpha_{em}}{\pi}\frac{1-x}{xy}\left\{A\sigma_T(Q^2,y) + B\sigma_L(Q^2,y)\right\} \approx \frac{\alpha_{em}}{2\pi}\frac{2-2y+y^2}{xy}\sigma_{\gamma p}^{tot}(ys) \quad (1.9)$$

where α_{em} is the electromagnetic coupling constant and $\sigma_T(Q^2,y)$ and $\sigma_L(Q^2,y)$ are the total photoproduction cross-sections using the transversely and longitudinally polarised virtual photons respectively.

Chapter 2

The H1 Detector

2.1 The HERA accelerator

The electron-proton colliding beam facility HERA (**H**adron **E**lectron **R**ing **A**nalage) consists of two independent accelerators designed to store 820 GeV protons and 30 GeV electrons (or positrons). These counterrotating beams are collided head on in four interaction points spaced uniformly around its 6.3 km circumference. Each of the electron and proton beams consists potentially of 210 bunches with a bunch crossing interval of 96 ns to give a designed luminosity of 1.5×10^{31} cm^{-2} s^{-1}.

The layout of the HERA accelerator can be seen in figure 2.1. The major detectors H1 and ZEUS are located at two of the four interaction points around the ring.

2.2 The H1 Detector

The H1 experiment is asymmetric in design with instrumentation for hadron detection biassed in the forward (proton) direction due to the difference in energy of the proton and electron. The possible reactions mentioned in the last chapter illustrate that the H1 detector is required to have good identification for leptons (especially electrons), high granularity and resolution for jets and good hermiticity to recognise missing transverse energy. Only with these properties is it possible for the detector

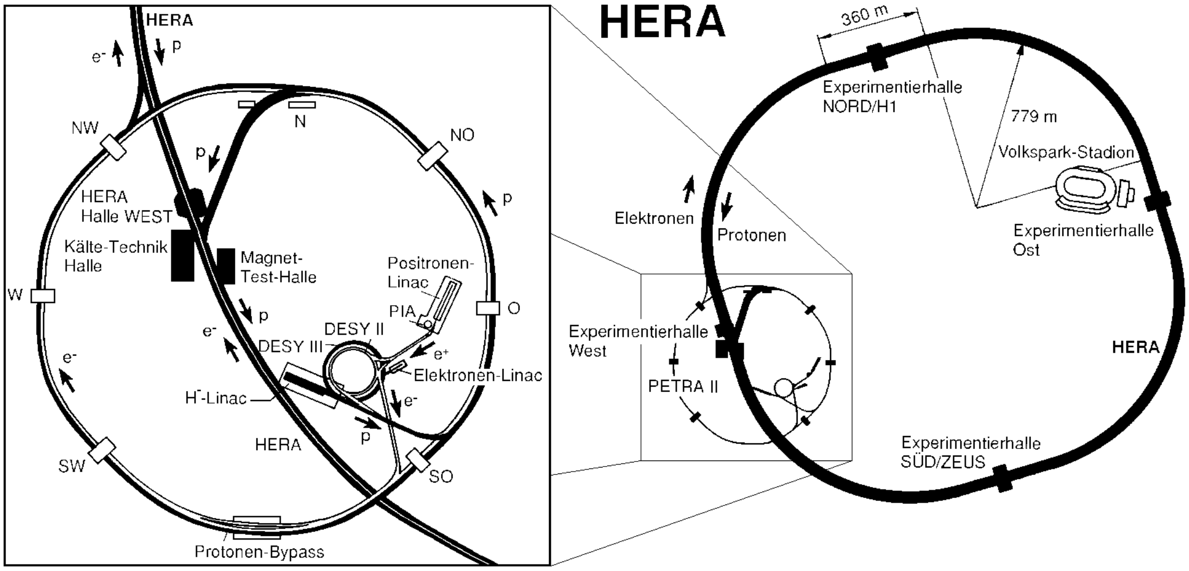

Figure 2.1: The layout of the HERA accelerator.

to record with adequate precision states that may contain several leptons accompanied by quark and gluon jets. The inclusive measurements of neutral and charged current interactions make heavy demands on the calorimeter, particularly in measuring electron energies. In addition, charmed hadron spectroscopy, charmed quark tagging, electron identification and charged particle reconstruction within jets require a high-resolution, large solid angle tracking system. The efficiency of all these subdetectors can only be fully exploited with a sophisticated triggering system which has to be able to overcome the adverse background conditions which are associated with an electron-proton collider.

The layout of the H1 Detector can be seen in figure 2.2. A right handed Cartesian coordinate system (x, y, z) is used or a spherical polar coordinate system (r, θ, ϕ). The direction of the proton beam is often referred to as the '*forward direction*' (positive z-values relative to the center of the interaction region and $\theta = 0$), and vice versa to that of the electron beam as the '*backward region*' (negative z and $\theta = \pi$).

The main components of the H1 detector are as follows:

- A tracking system detecting charged particles in the central region ($15° < \theta < 165°$) and the forward region ($7° < \theta < 25°$). There consist of drift chambers interspersed with multi-wire proportional chambers to give fast signals for triggers using charged particles originating from the event vertex. The central and forward tracking detectors (CTD and FTD) are used in conjunction with the multi-wire proportional chambers (MWPC) situated in the backward direction.

- A liquid argon (LAr) calorimeter which is designed to measure hadronic and electromagnetic energy flow. This surrounds the CTD and the FTD and is supplemented (in the backward direction) by Spacal which, as of 1995, replaced the backward electromagnetic calorimeter (BEMC). There is also a plug calorimeter which provides calorimetry at small angles in the forward direction.

- A superconducting coil and cryostat outside the hadronic calorimeter providing a magnetic field of 1.6 Tesla over the central region. This enables momenta values to be determined from the curvature of the tracks of charged particles.

- A set of iron plates surrounding the superconducting coil which acts as a return yoke for the magnetic field and which produces an almost uniform field parallel to the HERA beams. The return yoke is instrumented to allow measurement of hadronic energy and also to provide muon identification and tracking.

- A forward muon spectrometer which provides identification and measurement of muons in the forward region. It consists of a series of drift chambers positioned either side of a toroidal magnet.

- Two electromagnetic calorimeters (LUMI) are situated downstream in the electron beam direction and tag electrons and photons for the purpose of luminosity determination. They are also used to help detect the photoproduction background.

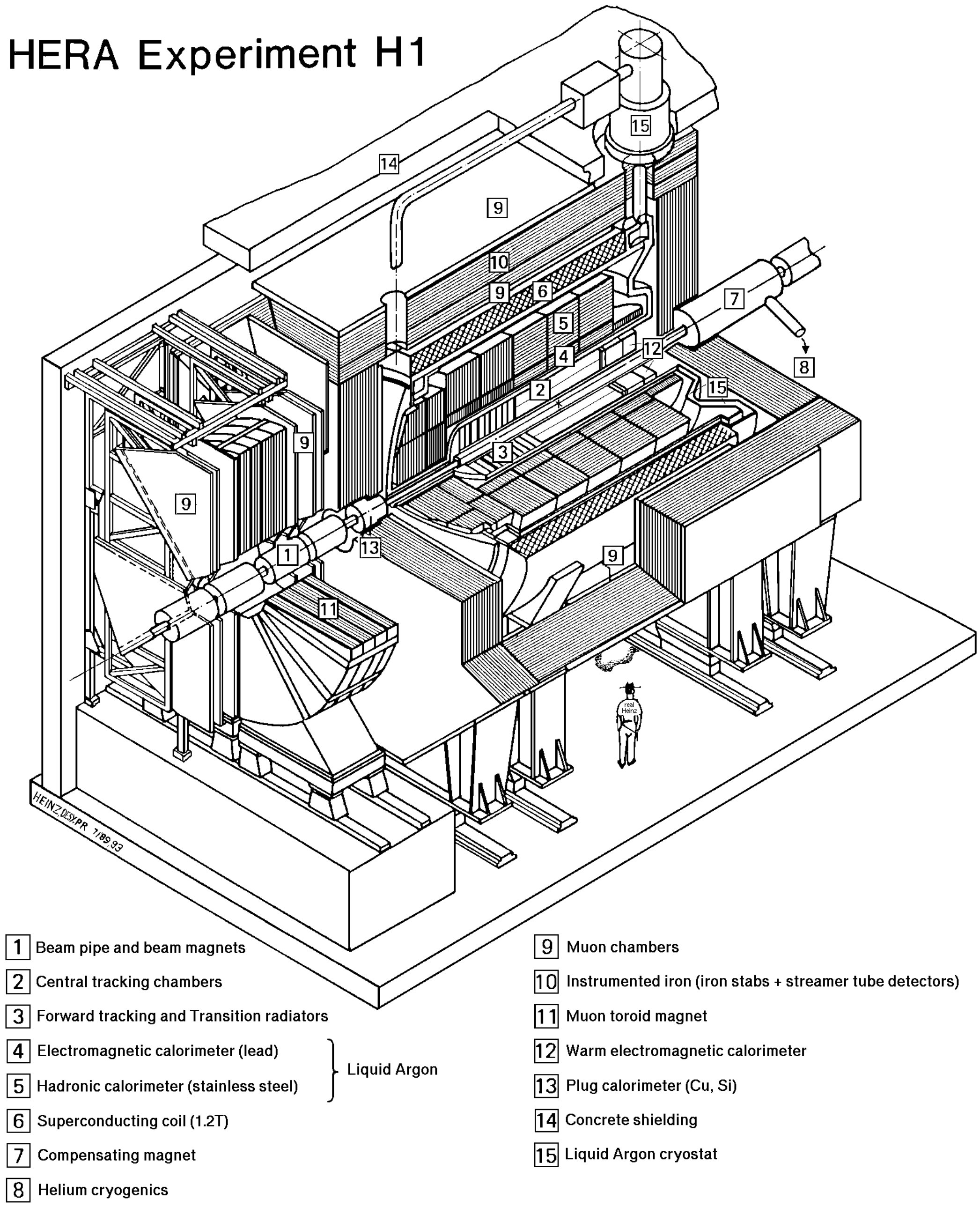

Figure 2.2: A 3D view of the H1 detector.

The rest of this chapter will be used to discuss in greater detail the aspects of the H1 Detector already mentioned above. Emphasis will be made on the components which are of particular relevance to this report. A detailed description of the H1 detector can be found in [9].

2.3 The H1 Tracking Detectors

The tracking system of H1 has been designed to reconstruct jets with high particle densities and to measure the momentum and angles of scattered isolated charged particles to a precision of $\sigma_p/p^2 \approx 3\times\ 10^{-3}$ GeV^{-1} and $\sigma_\theta \approx 1\,\mathrm{mr}$. Due to the large difference between the electron and proton beam energies many of the charged particles produced are in fact at a very low angle θ with respect to the incident proton beam direction. This is the motivation for the two separate tracking detectors, the CTD and FTD, the former with cylindrical chambers, the latter with planar chambers perpendicular to the beam axis. Each is optimised for tracking and triggering in its angular region and hence maintains a good efficiency for triggering and reconstruction over the whole solid angle. The transverse track momentum may be determined from the signals recorded in the drift chambers of the CTD and FTD and particle identification may be improved by measuring the specific energy loss dE/dx in the CTD drift chambers. A diagram illustrating a side view of the FTD and the CTD can be seen in figure 2.3.

2.3.1 The Forward Tracking Detector (FTD)

The design objectives for the FTD were as follows:

- momentum resolution for tracks with p >10 GeV/c constrained to the primary vertex of $\sigma_p/p^2 \approx 0.003$ (GeV/c)$^{-1}$;
- angular resolution better than 1 mrad;
- efficient track pattern recognition;

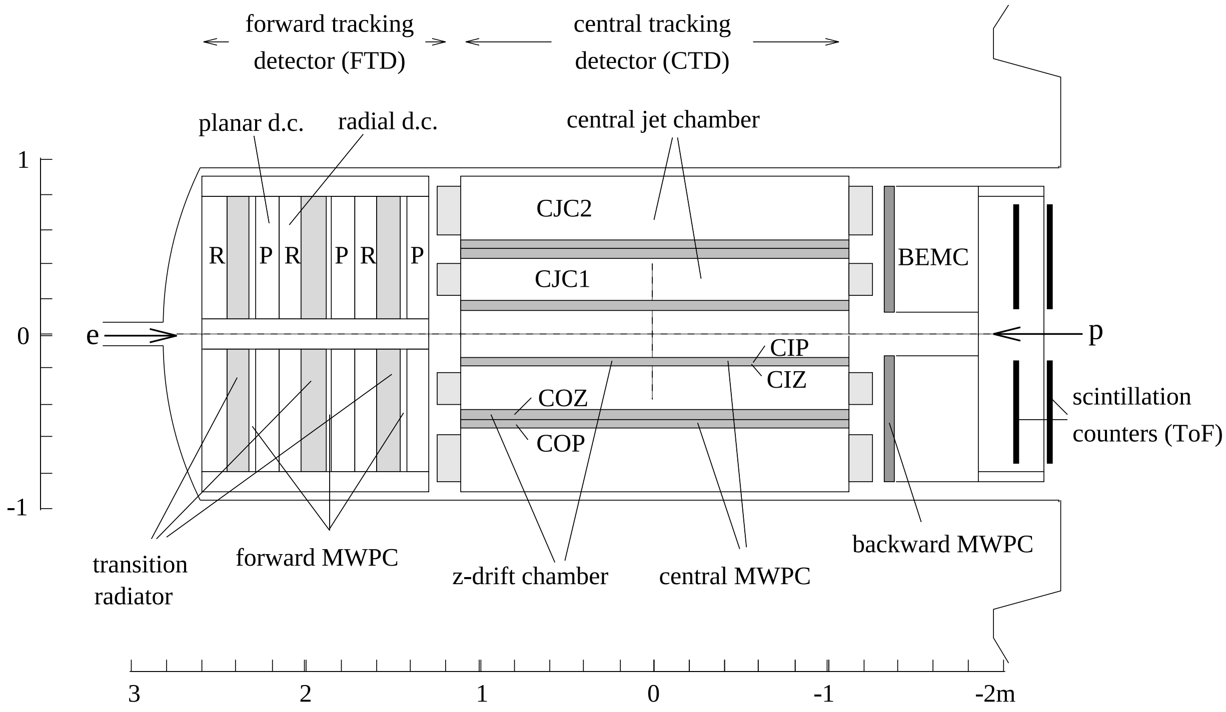

Figure 2.3: Side view of the H1 tracking detectors.

- efficient electron identification, with pion contamination below 10% for particle momenta up to 60 GeV/c;
- a fast ray trigger (provided by the MWPC's).

The detector consists of three identical sub-units known as Supermodules. Each Supermodule when viewed from the direction of the incoming proton consists firstly of three layers of Planar drift chambers, oriented at 0°, +60°, -60° to the vertical, followed by a MWPC, then a transistor radiator material, and finally a Radial drift chamber.

The Radial drift chambers are positioned at approximately 1.7, 2.1 and 2.5 m from the interaction point and consist of 48 wedge shaped segments. Each segment subtending 7.5° in ϕ and is equipped with 12 sense wires stacked in z. The Radial drift chambers are designed to make an accurate measurement of the azimuthal

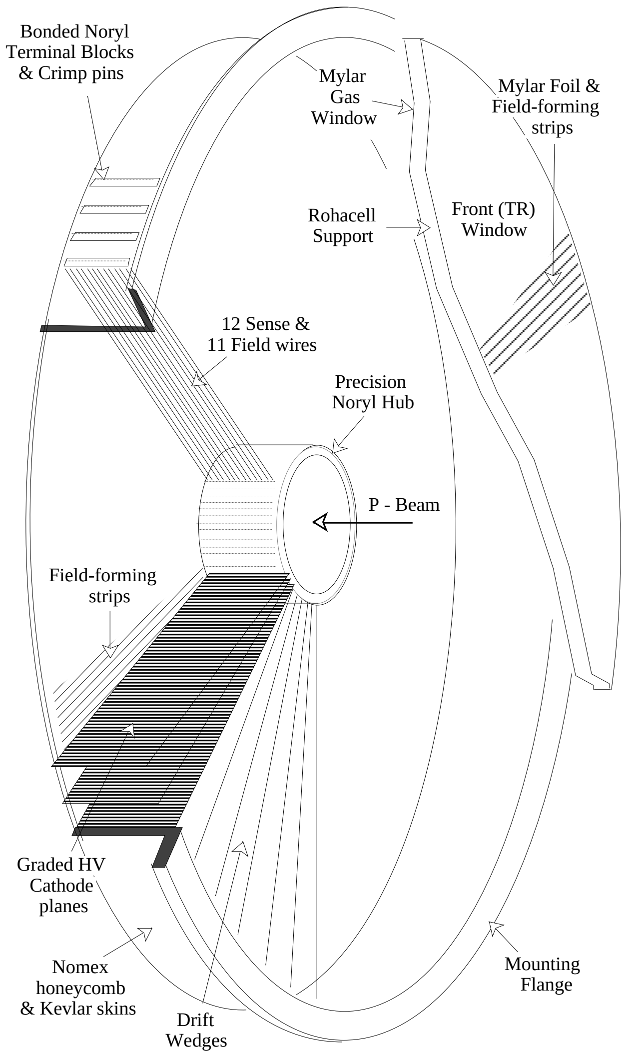

Figure 2.4: The Radial Drift Chambers.

angle, together with a moderate measurement of the radial coordinate using charge divisions. The layout of the Radial drift chambers is illustrated in figure 2.4.

The Planar drift chambers are positioned at approximately 1.4, 1.8 and 2.2 m from the interaction point. Each module consists of 12 planes of wires and each plane contains 32 parallel sense wires. These sense wires are only read out at one end and hence there is no knowledge of track position along the direction of the wire. However, the three orientations of the planes within a Planar chamber module enables the trajectory of a particle passing through the detector to be reconstructed.

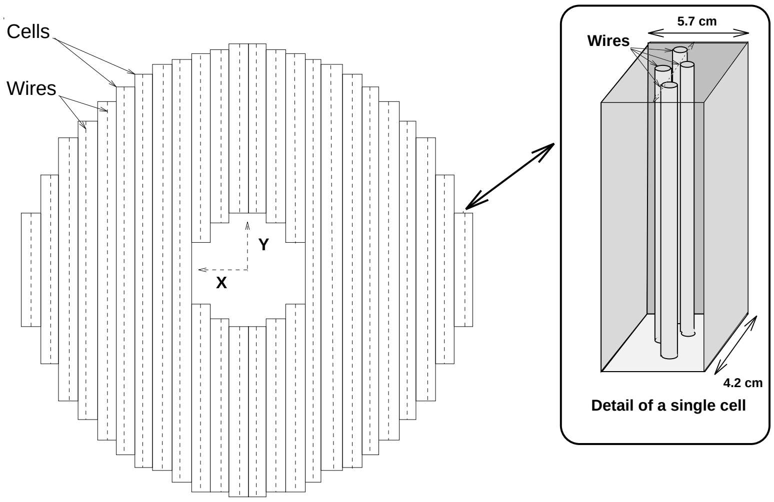

Figure 2.5: The Planar Drift Chambers.

The structure of the Planar drift chambers is illustrated in figure 2.5.

The three orientations of a Planar chamber module allow the reconstruction of a track segment that is well defined in both the radial and azimuthal directions. The resolutions of the FTD are 200 μm in the $r\phi$ plane and 170 μm in both the x and y coordinates.

2.3.2 The Central Tracking Detector (CTD)

The CTD is made up of two large concentric drift chambers called the CJC1 and CJC2 (collectively the CJC). The chambers have wires strung parallel to the beam axis (z-direction) with the drift cells inclined with respect to the radial direction by approximately 30°. The $r\phi$ measurement that can be provided by the CTD [10] has a resolution of 170 μm and, by comparing signals read out at both wire ends, a resolution of one percent of the wire length in z can be achieved. The CJC is a JADE type jet chamber, and has an inner radius of 200 mm, an outer radius of 795 mm and a length of 2640 mm centered about the nominal interaction point.

Complementing the measurement of charged track momenta in the central chambers are the central inner and the central outer drift chambers named CIZ and COZ respectively. The CIZ chamber fits inside CJC1, and the COZ fits in between CJC1 and CJC2. These two chambers deliver track elements with typically 300 μm resolution in z and 1 to 2% of 2π in ϕ. This requires a drift direction parallel to the beam axis and sense wires running perpendicular to the beam axis on the surface of the two cylinders with 180 and 4600 mm average radii. Linking these track elements to those obtained from the CJC with accurate $r\phi$ and moderate z information gives the final accuracy on both the longitudinal as well as the transverse momentum components.

Mounted inside the CIZ and the COZ respectively are two multiwire proportional chambers called the CIP and the COP. These chambers consist of a double layer of anode wires and are used to trigger tracks coming from a nominal interaction vertex.

2.3.3 The Backward MWPC

In the backward direction the reconstruction of the scattered electron in low Q^2 DIS events calls for an accurate track segment. This is given by the signals from four anode wire planes orientated at 45° to each other which make up the MWPC. The backward MWPC completes the trigger system for the tracking detector and also provides an additional space point for small angle tracks pointing in the backward direction.

2.4 The Calorimeters of H1

The task of the calorimeters is to measure the energy of the particles emerging from the interaction point. The calorimeter has a sandwich construction with separate layers of absorbing material (lead or steel) between sensitive detector regions. A particle passing through the calorimeter will interact with the material of the absorber, generating secondary particles which will themselves generate further particles. This continues such that a *cascade* or *shower* develops. Measurement of the amount of ionisation in the sensitive detector region enables the energy of the incident particle to be determined.

Detection and measurement of electrons together with very good performance in the measurement of jets with high particles requires the calorimeter to be inside the large coil providing the magnetic field. This tends to minimizes both the amount of dead material in front of the electromagnetic calorimeter and the overall size and weight of the calorimeter. A diagram illustrating the calorimetry system of H1 can be seen in figure 2.6.

2.4.1 The Liquid Argon Calorimeter

Liquid argon was chosen as a result of the following:

- stability and ease of calibration;
- fine granularity for e/π separation and energy flow measurements;
- and homogeneity of response.

The liquid argon calorimeter (LAC) [11] covers the polar angular range between $\theta = 4°$ and $\theta \approx 153°$. It is segmented into a hadronic part and an electromagnetic part and is divided along the beam pipe into eight self supporting 'wheels'. Each of the six barrel wheels are segmented, in ϕ, into eight identical stacks or octants. Studies have shown that the energy resolution (σ_E/E) of the LAC is approximately $12\%/\sqrt{E}$ (E in GeV) for the electromagnetic section and approximately $50\%/\sqrt{E}$ for the hadronic section (plus constant terms of 1% and 2% respectively).

2.4.2 The Backward Electromagnetic Calorimeter (BEMC)

The BEMC was originally the part of the H1 calorimetry system that covered the angular range of $151° \leq \theta \leq 177°$. In 1995 it was replaced by the Spacal which is described in section 2.4.3. The BEMC was designed to measure the energy of electrons scattered in the backward region and also provides limited coverage of

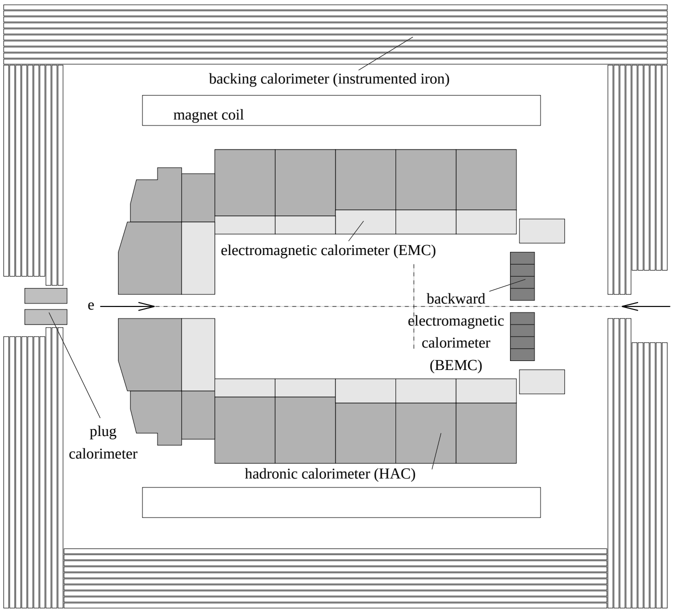

Figure 2.6: The Calorimetry system of the H1 Detector

hadronic energy flow in photoproduction events. Test beam studies have determined the electromagnetic energy resolution of the BEMC to be approximately $10\%/\sqrt{E}$ (constant term of 1%) [12].

2.4.3 SPACAL

The SPACAL (**SPA**getti **CAL**orimeter) provides calorimetry in the backward region. The main task of this new calorimeter is to provide precise measurement of the scattered electron energy and improve the quality of hadronic energy measurements. The SPACAL, unlike BEMC, consists of two sections - electromagnetic and hadronic. Both of these sections consist of scintillating fibers inserted into lead.

Test beam studies have shown that the electromagnetic section has an energy resolution of approximately $7\%/\sqrt{E}$ (constant term of 1%) [13] and the hadronic section has an energy resolution of approximately $56\%/\sqrt{E}$ [14] for hadrons and $13\%/\sqrt{E}$ for electrons (plus constant terms of 3% and 3.6% respectively).

2.4.4 The PLUG Calorimeter

The major aim of the PLUG calorimeter is to minimize the missing part of the total transverse momentum due to hadrons at small angles. The PLUG signal is also useful to detect the presence of energy flow in the very forward region of the H1 detector. The detector itself consists of layers of copper absorber plates interleaved with layers of silicon detectors, and has a resolution of approximately $150\%/\sqrt{E}$.

2.5 The Detection of Muons

Two detectors are involved in the detection of muons at H1. Firstly, there is the instrumented iron which detects muons emitted in all directions and secondly there is the forward muon detector which is situated in the forward direction. The latter provides an independent momentum measurement and can be used in conjunction with the FTD. Muon identification provides information that is particularly useful for heavy flavour physics and the search for new and exotic particles.

2.5.1 The Instrumented Iron

The iron return yoke that is surrounding the superconducting solenoid and all the major detector components of H1 is instrumented with limited streamer tubes (LST). When closed, the iron yoke consists of flat end-caps and an octagonal barrel. Measurements made in the barrel region are defined by spherical polar coordinates (r, θ, ϕ) whereas the coordinates used in the end-caps are Cartesian (x, y, z).

The iron yoke is segmented into 10 iron plates of 7.5 cm thickness and instrumented with 16 layers of LST. Five of these layers are equipped with strips perpendicular to the wire direction to measure the coordinate along the wire and the other 11 with large rectangular pads for a coarse energy measurement. Using the wire signals the position of a passing muon can be determined with a resolution of about 3-4 mm and the strips give a resolution of about 10-15 mm in the perpendicular direction. The pads provide a space-point with an accuracy of about 10 cm. A cross-sectional view through the instrumented iron is shown in figure 2.7.

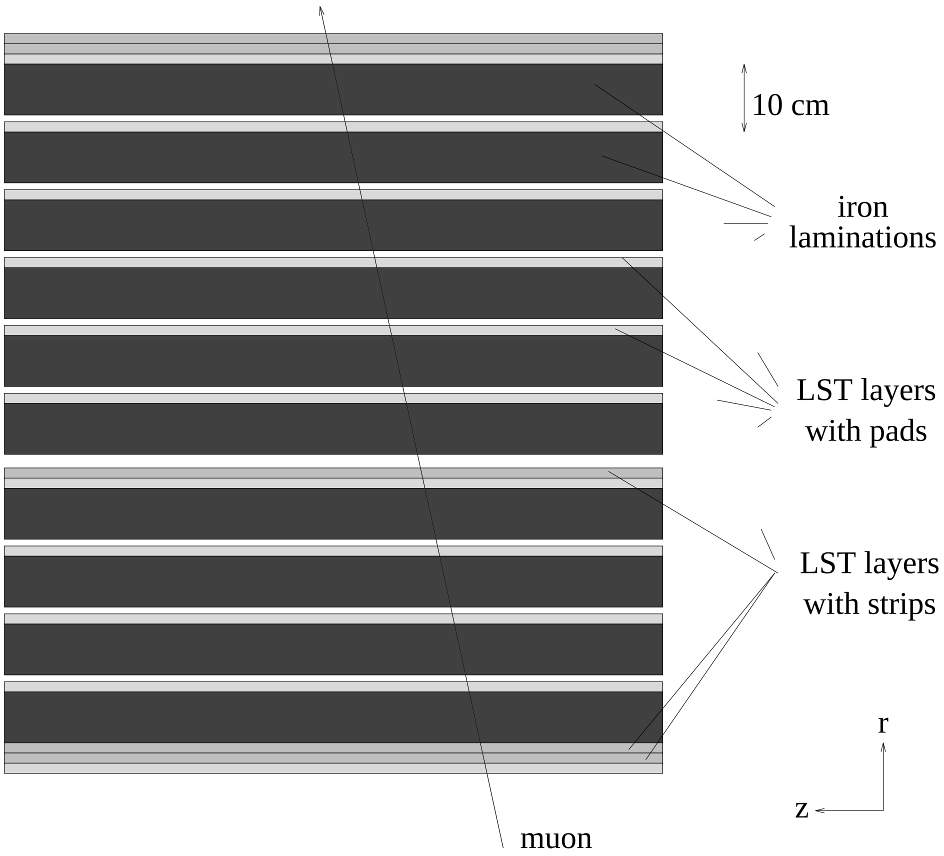

Figure 2.7: Cross-sectional view through the instrumented iron.

2.5.2 The Forward Muon Detector

The forward muon detector (FMD) [15] measures high energy muons in the angular range of $3° \leq \theta \leq 17°$. The detector consists of drift chamber planes mounted on either side of a toroidal magnet. The toroidal magnet consists of 8 solid iron modules built into mobile half-toroids for access reasons. The inner radius of the toroid is 0.65 m, the outer radius 2.90 m, and the length between the flat ends 1.2 m. The field varies with radius, from 1.75 T at the inner radius to 1.5 T at the outer radius.

The drift chamber planes, which increase in size from about 4 m in diameter for the first detector plane to 6 m in diameter for the last, are all divided into octants of individual drift cells mounted on aluminium frames. The orientation of the drift cells is such that four of the planes measure the polar angle (the θ layers) and by measuring the track bending in the toroid determine the momentum of the particle,

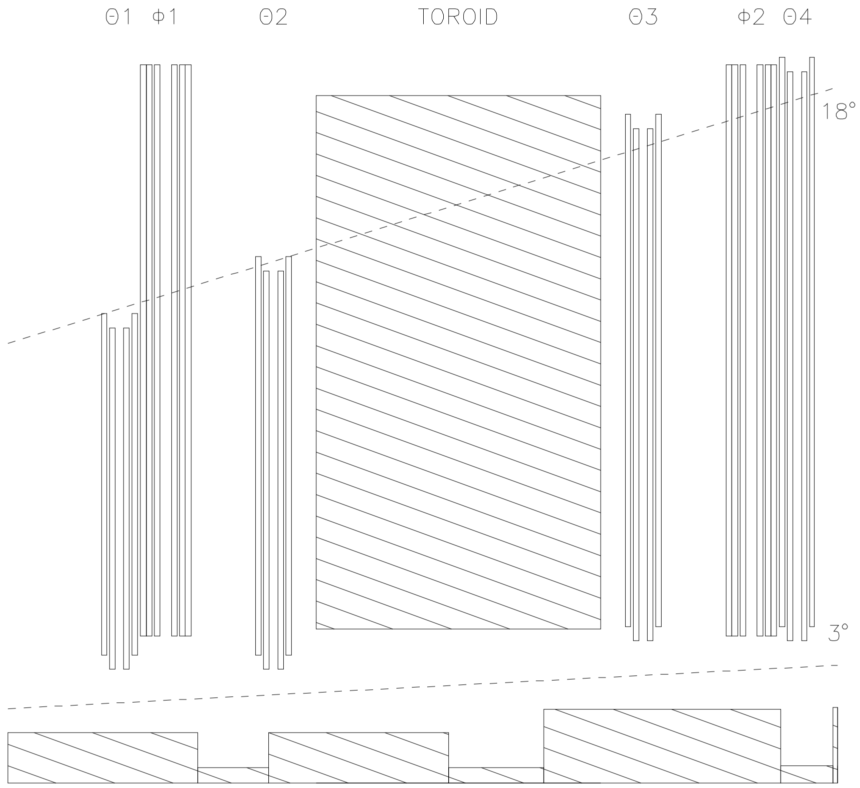

Figure 2.8: Cross-sectional view of the forward muon system.

while the remaining two planes measure the azimuthal angle (the ϕ layers). Each plane consists of a double layer of drift cells which are staggered by half a cell width. This arrangement enables the resolution of left-right ambiguities and determination of *t-zero* (the global timing offset for the detector). The momentum resolution is limited by the energy loss and multiple Coulomb scattering in the magnet iron and at 5 GeV/c is 22% and deteriorates slowly to 36% at 200 GeV/c.

A diagram showing the positioning of the ϕ and θ layers of the FMD can be seen in figure 2.8.

All drift cells contain a central sense wire which at one end is connected to an adjacent cell by a 330Ω resistor and at the other is connected to a preamplifier. This allows not only a determination of the track position transverse to the sense wire from the measurement of the drift time but the position along the wire by a charge division measurement. Charge division along the wire gives a measurement

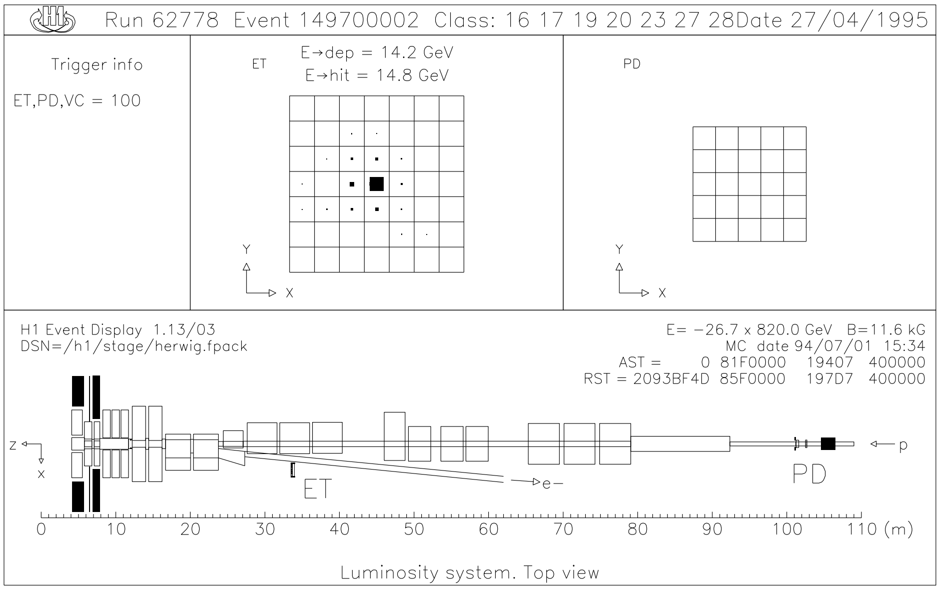

Figure 2.9: The H1 Luminosity System.

approximately accurate to 1% of the length of the sense wire. The observed drift distance resolution is between 300 and 400μm.

The gas used in the chambers is fast enough for the pulse to arrive in time for the trigger and is also non-inflammable for safety reasons. The gas mixture that is currently used in the chambers is 92.5% Argon, 5% Carbon Dioxide and 2.5% methane.

2.6 Luminosity Monitoring

The luminosity system is designed to make a fast relative luminosity measurement with a statistical precision of $\approx$ 2% s^{-1} at nominal conditions. The luminosity is determined from the rate of the Bethe-Heitler events $ep \longrightarrow ep\gamma$ which have a precisely calculable cross section and make them ideal for the determination of the luminosity. An energy measurement for small angled scattered electrons and photons can be made by calorimeter detectors down stream in the electron direction. The layout of the H1 luminosity system can be seen in figure 2.9.

2.7 Triggering

The high bunch crossing rates coupled with high beam background rates lead to the requirement of a sophisticated trigger and data acquisition system. Background events can be several orders of magnitude higher than the *interesting* physics events so it is important that these events are identified separately. Typical background events are as follows:

- proton beam-gas interactions;
- proton beam-wall interaction;
- cosmic muons;
- beam halo muons;
- low energy photons or electrons from synchrotron radiation.

The data event selection is divided into five levels, the first four involving four levels of triggering: L1, L2, L3 and L4. The fifth level, L5, is where the reconstruction of the data occurs and this will be described in detail in Chapter 3.

The triggers in L1 to L4 examine the information from the various subdetectors of H1 and select events satisfying any one of a number of pre-set combinations of conditions. These conditions are know as 'subtriggers' which are made up from 'trigger elements'. Trigger elements are the digital information that are sent from the individual subdetector triggers to the Central Trigger. Subtriggers are logical expressions, with the trigger elements as arguments.

The first selection procedure, L1, examines the information for every bunch crossing. If any of the subtrigger conditions are satisfied then the event is kept. If the experiment is to be efficient in its use of the luminosity of HERA the L1 triggers must either select the interaction of interest in less than 96 ns or be able to operate in a 'pipeline' mode. The method of pipelining basically means that the information from 27-35 bunch crossings can be simultaneously stored so that the allowed processing time is extended. The number of steps in the pipeline determines the *latency* of the trigger, which is the delay between the time of the actual bunch crossing and the L1 decision being produced. A further requirement of the L1 trigger is that it must be able to carry out the procedure referred to as t-zero extraction. This means that it must be able to identify each selected interaction with an unique bunch crossing. Hence, in any combination of L1 trigger conditions, at least one trigger element must be based on a detector which has intrinsic time resolution better than the bunch crossing period of 96 ns.

The L2 and L3 triggers are more sophisticated than L1 and at present have not been installed. However, if an event is not rejected then all the detector output is passed on to the central data acquisition system so that an L4 decision can be made. L4 is a farm of computers with a processing capability of about 100 events per second. Decisions are made within approximately 1 μs and a few hundred μs by the L1 and L4 triggers respectively.

The Forward Muon Trigger (FMT) makes up part of the L1 trigger and will be discussed in Chapter 5 of this report.

Chapter 3

Track Selection

To produce a 'good' track selection for analysis purposes it is necessary to understand important aspects of the track reconstruction in the FTD, FMD and instrumented iron. This chapter attempts to describe the reconstruction in each of the three detectors and then, using it as a basis, a set of cuts are made to define 'good' tracks.

3.1 Forward Track Reconstruction

Major changes were made to the track reconstruction of the FTD in 1994 and the updated reconstruction is described in detail in [16]. The principal difference is in the reconstruction of the planar track segments. As described in Chapter 2, the Planar chambers are mounted in three orientations, each of which has 4 wire planes. Readout is only obtained from one end of each wire so the positions along the wire are not measured. Therefore at least two orientations are required to define a line track segment and a third orientation is needed, as confirmation, to reduce the large hodoscope ambiguity. The reconstruction requires a planar track segment to consist of at least three hits from each orientation (i.e. at least nine hits per planar track segment) and are referred to as *primary* segments. The original reconstruction used to stop at this point. Now attempts are made to find additional track segments by relaxing the requirement on the number of hits to form what are called *secondary* and *tertiary* segments. Secondary segments have three hits in two orientations with only one or two hits in the third. Tertiary segments only have two hits in two of the three orientations.

Primary segments are obviously more reliable than secondary segments which are in turn more reliable than tertiary segments. Even if unattached to other segments the primary and secondary segments are treated as tracks; however tertiary segments are only used to form a track when the track contains either a primary, or a secondary planar segment, or a radial segment with at least six hits.

Forward track selection is based on the number of planar track segments and whether they are primary, secondary or tertiary. For high multiplicity events in the forward direction both the efficiency of the track reconstruction and the track quality deteriorates because a large fraction of the planar track segments that are reconstructed are due to false combinations of the three orientations. Rejection of these can be achieved by requiring that there are at least two planar track segments reconstructed since they then have to be linked. Low multiplicity events do not need such a requirement as the planar track segments are typically of a higher quality.

3.2 Instrumented Iron Track Reconstruction

During track reconstruction all the information available from the 16 wire, 5 strip and 11 pad layers is used. The track resolving power is greater for the wires so pattern recognition starts with them. The wires give a measurement in y only. Hence, if curved track candidates are to be reconstructed, hits must also be found in the strip layers which give a measurement in x. Matched hits in the wires and strips are then combined to give a three dimensional track and any ambiguities are resolved by using the pad information. To reconstruct a track, at least three wire layers are required. The track fit, using an average value for the magnetic field inside the iron plates, performs a least square fit simultaneously to wires and strips. The energy loss in one plate is at least 80 MeV and this is also taken into account by an iteration procedure.

In the barrel region muons with energies below 2 GeV stop within the iron and

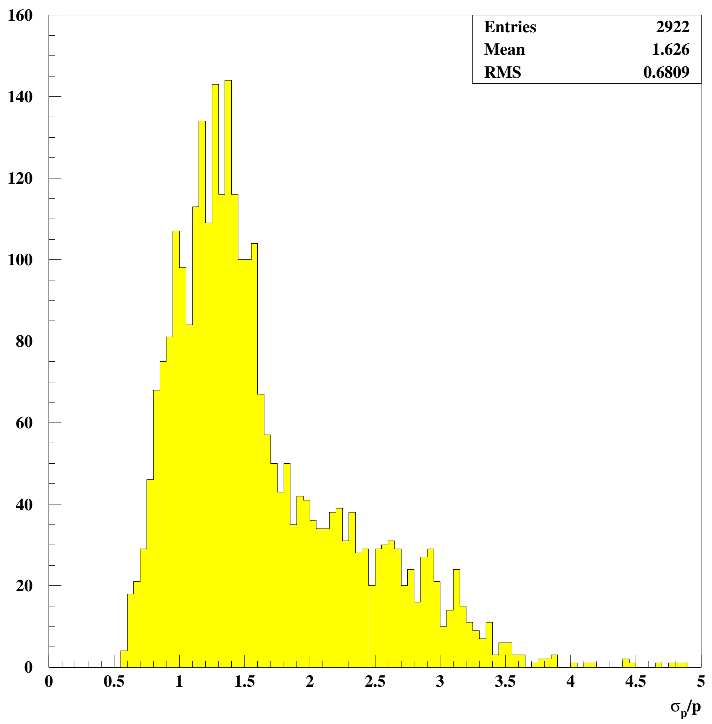

Figure 3.1: Momentum resolution of the Instrumented Iron.

in the forward direction end-cap the effective threshold is 2.5 GeV.

The momentum of the passing muon can be estimated by using the field in the return yoke iron and the curvature of the track. However, it is not always possible to calculate the momentum of the track in the iron. Figure 3.1 shows a plot of the momentum resolution of the instrumented iron. The resolution is approximately 160% which indicates that the momentum determination within the iron is highly inaccurate. For this reason, the main aim is to use the reconstructed track direction in the iron to identify a track in the FTD as a muon.

3.3 FMD Track Reconstruction

The FMD track reconstruction identifies the trajectory of muons and then associates a momentum value to each of them.

Before a track can be fully reconstructed a three step procedure must be carried out [17] :

1. pairs are formed using the hits found in the double planes of each octant;
2. pairs are linked to form *track segments*;
3. pre- and post- toroid track segments are linked together to form a track with an associated momentum.

3.3.1 Pair Finding

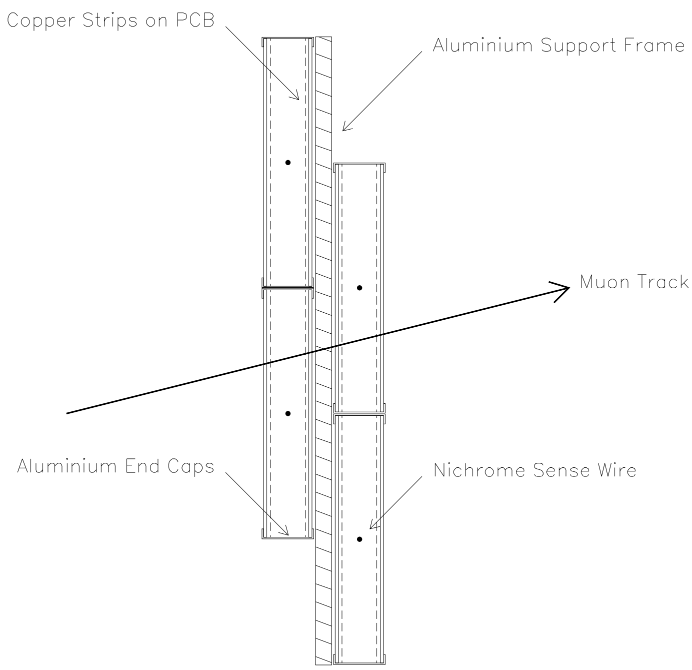

Figure 3.2: Cross-sectional view through cell.

A cross section of cells mounted on an octant frame can be seen in figure 3.2. The cells of each plane are displaced from each other by half a cell width. This staggering of the cells helps to resolve the 'left-right' ambiguity in the drift coordinate for a pair of hits. 'Pairs' are only found if the difference in the drift coordinate of the two hits fall within 3.42 cm. This corresponds to an angular acceptance of $\pm 45°$. Unpaired hits are kept and are considered in the track segment reconstruction.

3.3.2 Track Segment Reconstruction

The previously found pairs (and single hits) are now linked in the two θ layers (see figure 2.8) on each side of the toroid. Pre-toroid track segment reconstruction[1] starts by choosing a pair of hits in an octant of layer θ_1 and any pair of hits or a single hit in the same octant of layer θ_2. A straight line fit is made and a χ^2 value determined by using both the drift and charge division information. Track segments are only kept if the χ^2 value is below a certain cut.

If a pair of hits or single hit in the ϕ layer is found to correlate with a track segment of the θ layers then the previously defined track segment is refitted to give a new χ^2 value. Again this is subjected to a χ^2 cut. A track segment is fully reconstructed when the fit is made to all the points that have been found in each of the three chambers.

3.3.3 Pre- and Post-toroid Track Segment Linking

To construct a full track a pre-toroid track segment and a post-toroid track segment must be linked together. A first step is to extrapolate the track segments into the central plane of the toroid and calculate the difference in both r and θ. Only track segments that are sufficiently close are considered for the full track segment linking procedure.

Each track segment is assigned 52 possible momentum values and every value is extrapolated through the toroid. In order to follow the path of the muon through the toroid the energy loss and bending of the muon trajectory due to the magnetic field must be both taken into account. The track segments on the other side of the toroid are then fitted to every exit point of the extrapolated track segments and a χ^2 value determined for each pair of segments. A plot of χ^2 as a function of momentum is built up. The value of momentum with the smallest χ^2 associated with it is taken as an estimate of the momentum of the muon on entering the toroid. If there is no momentum value with a χ^2 below a pre-set threshold then the pair of track segments

[1] Post-toroid track segment reconstruction is identical except that it starts with the θ_4 layer.

are not linked.

Further improvement can be made to the value determined for the momentum by fitting a quadratic function to the χ^2 distribution. The fit uses the smallest χ^2 value and the two adjacent χ^2 values. The minimum of this function is the momentum which is finally taken and the second derivative at the minimum is used to make an estimate of the uncertainty of the reconstructed momentum.

A muon quality parameter is also defined which is dependant on the type of minimum that is found. This parameter can have the values 1 to 5 which are set as follows:

1 = A minimum found using all information that is available (x, y, θ, ϕ).

2 = A minimum found using only θ and ϕ information.

3 = A minimum found using only x and y information.

4 = A minimum found, however the track exits the toroid so the momentum measurement is unreliable.

5 = A minimum found at the lowest momentum value of the scan. This gives an inaccurate momentum measurement (no minimum), but the charge is normally correct.

The above procedure is repeated for every pair of pre- and post-toroid track segments. If a single track segment is found to be part of two or more reconstructed tracks then only the track with the lowest muon quality value or lowest χ^2 value associated with it will be kept. Any track segments used in alternative fits will be rejected.

The final momentum resolution is limited by the multiple Coulomb scattering and the energy loss of the muon in the toroid. This gives a momentum resolution of approximately:

$$\sigma_p/p \approx 0.22. \tag{3.1}$$

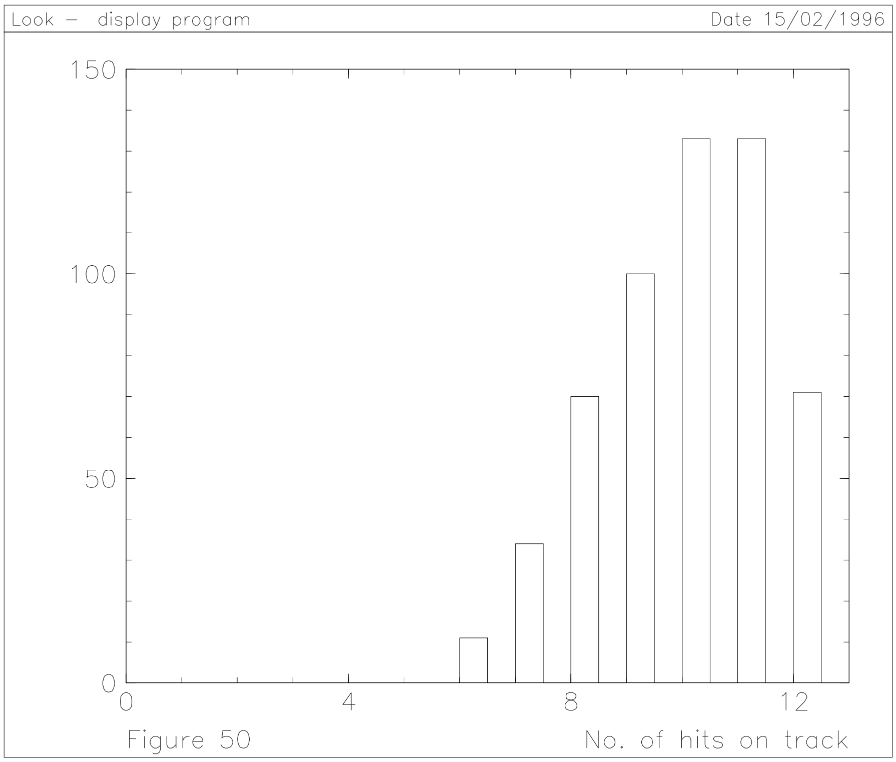

Figure 3.3: L5 histogram showing the number of hits detected in the FMD.

A fully reconstruction track will have $6 \leq \text{hits} \leq 12$, where there are a maximum of two hits in each of the double layers.

Figure 3.3 shows a L5 histogram of the number of hits detected in the FMD.

3.4 Class 24 Events

For data events to be stored on Data Summary Tapes (DST's) they must first be preselected into 'classes'. There are 32 different event classes. Class 24 events contain at least one good inclusive muon or electron. The following cuts define the class 24 selection for muons:

CTD Track Cuts

A 'good' quality CTD track is defined by the following cuts:

- $p \geq 0.8\,\text{GeV/c}$;

- minimum number of hits allowed to reconstruct a track = 10;
- The radius at the start of the track (R^{start}) $\leq 30\,\mathrm{cm}$;
- The measured z value at the point which is closest to the vertex when the track is extrapolated back to the vertex ($z0$) $\leq 40\,\mathrm{cm}$;
- The maximum fraction of unused hits per track = 0.3.

FTD Track Cuts

A 'good' quality FTD track is defined by the following cuts:

- χ^2 of vertex ≤ 20;
- χ^2 of track ≤ 10;
- p $\geq 1.0\,\mathrm{GeV/c}$;
- $\theta \geq 0$;
- Number of Planar Supermodules registering hits ≥ 1;
- For tracks in the angular region of $\theta \leq 20^\circ$ the total sum of the number of Planar Supermodules + Radial Supermodules registering hits ≥ 2;
- $z0 \leq 40\,\mathrm{cm}$;
- The radial distance of a non-vertex fitted track at the vertex (R_0) $\leq 5.0\,\mathrm{cm}$.

Iron Quality Track Cuts

These cuts are dependent on whether the track is found in the barrel or the end-cap. The following cuts are made on the iron tracks in the barrel:

- maximum number of the first wire layer recording a hit = 5;
- minimum number of layers with recorded hits = 2;
- $z0 \leq 100\,\mathrm{cm}$.

The cuts made on the iron tracks in the end-cap region are as follows:

- minimum number of layers with recorded hits in the forward end-cap = 6
- minimum number of layers with recorded hits in the backward end-cap = 3
- maximum number of the first wire layer recording a hit = 8.

A further cut, which is common to barrel and iron-cap iron tracks, is the requirement that the iron track when extrapolated back to the vertex position, the nearest point to the beam axis falls within a 100 cm region around the nominal vertex.

FMD Track Cuts

- the intersection of the pre-toroid track segment in the rz plane with the z axis (r=0) is given a maximum value of 300 cm and a minimum value of -400 cm;
- the difference in the ϕ coordinate of the entry and exit points to and from the forward muon system has a maximum value of 1.0 radians (57.3°);
- muon quality = 1 or 2;
- $\chi^2 \leq 20.0$.

3.5 The Removal of Bad Tracks

Good tracks used in the analysis in Chapter 4 are defined by cuts made on the reconstructed tracks and are specific to the CTD, the FTD and the iron detectors.

The track selection has two main objectives :

- the removal of 'bad' tracks;
- the removal of unwanted hypotheses.

3.5.1 Track Cuts

The iron track quality cuts made in this track selection are essentially the cuts that define class 24 events which have been described in section 3.4.

For central track selection a variable is introduced called DCA$'$ which represents the corrected *distance of closest approach*. This uses the point at which the event actually occurs instead of the nominal event vertex which has the coordinates (0,0). Track length is also introduced which is defined as R^{stop} - R^{start}, where R^{start} is the radius value at the start of the track and R^{stop} is the radius value at the end of the track.

In some instances two tracks detected in the CTD are found to be track segments of the same physical track. This effect occurs for at least 12% of all events on DST [18] and to prevent double counting one of the tracks must be rejected. This is done by considering the transverse momentum (p_t), θ, ϕ and the radius values of the track. Cuts are made on these variables to ensure that the best track of the two is kept.

Forward tracks cuts use the χ^2 values of the track fit (χ^2_{DTNV}) and of the vertex fit (χ^2_{DTRA}). The subscripts DTNV and DTRA are the names given to DST tracking banks. The DTRA bank contains all vertex fitted tracks including multiple fit hypotheses (which are discussed in section 3.5.2) and the DTNV contains all non-vertex fitted tracks. A further cut is also made on the variable R_0 which represents the radial distance of a non-vertex fitted track at the vertex.

The chosen set of cuts are as follows:

Cuts on Central Tracks

- $p_t > 150\,\mathrm{MeV/c}$;
- $25° < \theta < 155°$;
- Track Length $> 10\,\mathrm{cm}$;
- $\mid \mathrm{DCA}' \mid < 2\,\mathrm{cm}$;

- 'Double' Tracks removed.

Cuts on Forward Tracks

- $p_t > 150\,\mathrm{MeV/c}$;
- $6^\circ < \theta < 25^\circ$;
- $\chi^2_{DTNV} < 25$;
- $\chi^2_{DTRA} < 10$;
- $R_0 < 10\,\mathrm{cm}$;
- Number of Planar Segments (primary + secondary) > 0.

3.5.2 Hypothesis Removal

A CTD track reconstructed in the acceptance region of the FTD (i.e. $16^\circ < \theta < 25^\circ$) can be linked to a FTD track; this is know as a *combined* track. The cuts that are applied to combined tracks are essentially an amalgamation of the set of cuts applied to CTD and FTD tracks.

Multiple fit hypotheses arise because the same track can be linked to several vertices or a central track can exist with and without a forward track. In the case of a combined track the tracking bank will consist of three entries corresponding to the 'forward', 'central' and 'combined' tracks which are hypotheses of the same physical track. In order to prevent double counting the best hypothesis must be chosen. Combined tracks containing information from both the forward and the central tracks are usually chosen [19] in preference to central tracks which are chosen in preference to forward tracks.

Chapter 4

Muon Detection in the Forward Direction

Muon detection has been studied most fully in the angular region $30° < \theta < 167°$. In this region the muons pass through the central tracker, the calorimeter and the instrumented iron. This chapter concentrates on the acceptance of the 'forward region' as defined by the angular region $3° < \theta < 20°$. A muon traveling in this direction may be detected in the following detectors:

- the Forward Tracking Detector (FTD);
- the Instrumented Iron (forward end-cap);
- the Forward Muon Detector (FMD).

It is essential that the linking between each of these detectors is correct and in this chapter an attempt to resolve any ambiguities in the linking has been made.

4.1 Data Samples

The data samples used for this analysis are the following:

- 1995 DST data which has been selected using the class 24 cuts. The selection requires that each event contains at least one muon in the forward direction. The sample contains approximately 9000 events.

- Single muon Monte Carlo in which all the muons that are generated lie within the angular region of $2^\circ \leq \theta \leq 20^\circ$ and have a momentum value in the range $5\,\mathrm{GeV/c} \leq p \leq 50\,\mathrm{GeV/c}$. There are approximately 60,000 events in this sample.

- DST Monte Carlo of the following decay:

$$\chi \longrightarrow J/\psi + \gamma \longrightarrow \mu^+\mu^- + \gamma. \tag{4.1}$$

  This sample contains approximately 10,000 events which have an angular distribution covering the whole of the H1 detector. The number of these events which contain a detectable muon in the forward direction is approximately 36%.

4.2 Link Hypothesis Removal and the Selection of 'Best' Links

In high multiplicity events there are often several tracks in one of the detectors 'linked' to a track in another. Removal of the invalid 'link' hypotheses is attempted in two ways; either by making a choice on the probability of the link or by making a choice on the transverse momentum of the FTD track. First the link with either the best probability value or the highest FTD transverse momentum (p_t) is selected. Any other links which have a common FTD, FMD or iron track will be discarded. The remaining links that are unique to the previously chosen link go through the same selection and rejection procedure. This continues until all links have been assessed.

4.3 Results

4.3.1 The Momentum Resolution of the FMD

Figure 4.1 shows the momentum resolution for the FMD for (a) data and for (b) the $\chi \longrightarrow J/\psi + \gamma$ Monte Carlo. It can be seen that the Monte Carlo momentum resolution is about 18 %, while for data it is 16 %.

Figure 4.1 (c) and (d) show the same variable plotted against the FMD track momentum (the vertical axis). Unlike the data, the majority of Monte Carlo events are in the region where the FMD momentum is greater than 4 GeV. Hence, this accounts for the difference in the mean resolutions of the data and Monte Carlo.

Low momentum muon tracks below approximately 2.3 GeV/c are difficult to reconstruct since the energy loss when transversing the toroid imposes a minimum reconstructable momentum (see section 4.3.2). Reconstruction is further inhibited by the large bending of the muon trajectory when transversing the toroid. This causes pre- and post-toroid track segment linking to become difficult since there is an increase in background that can be linked to real track segments.

Figure 4.1 shows that, for muon tracks with a momentum value less than 3 GeV/c, the width of the data distribution is slightly larger than that for Monte Carlo. However, it should be noted that the difference is small and the overall agreement for the momentum resolution of the FMD between data and Monte Carlo is good.

4.3.2 Energy Losses

Muons entering the FMD have first to pass through the FTD, the electromagnetic and hadronic calorimeters and the instrumental iron. In doing so they suffer multiple Coulomb scattering and energy loss in the media and bending in the field of the H1 solenoid magnet and return yoke. The size of both effects are dependent upon the momentum of the muon such that muons with a momentum of less than approximately 3 GeV/c cannot reach the FMD at all. Muons which do enter the FMD suffer further energy losses due to the iron of the toroid.

Figure 4.2 shows (a) the energy loss in the toroid and (b) the energy loss in

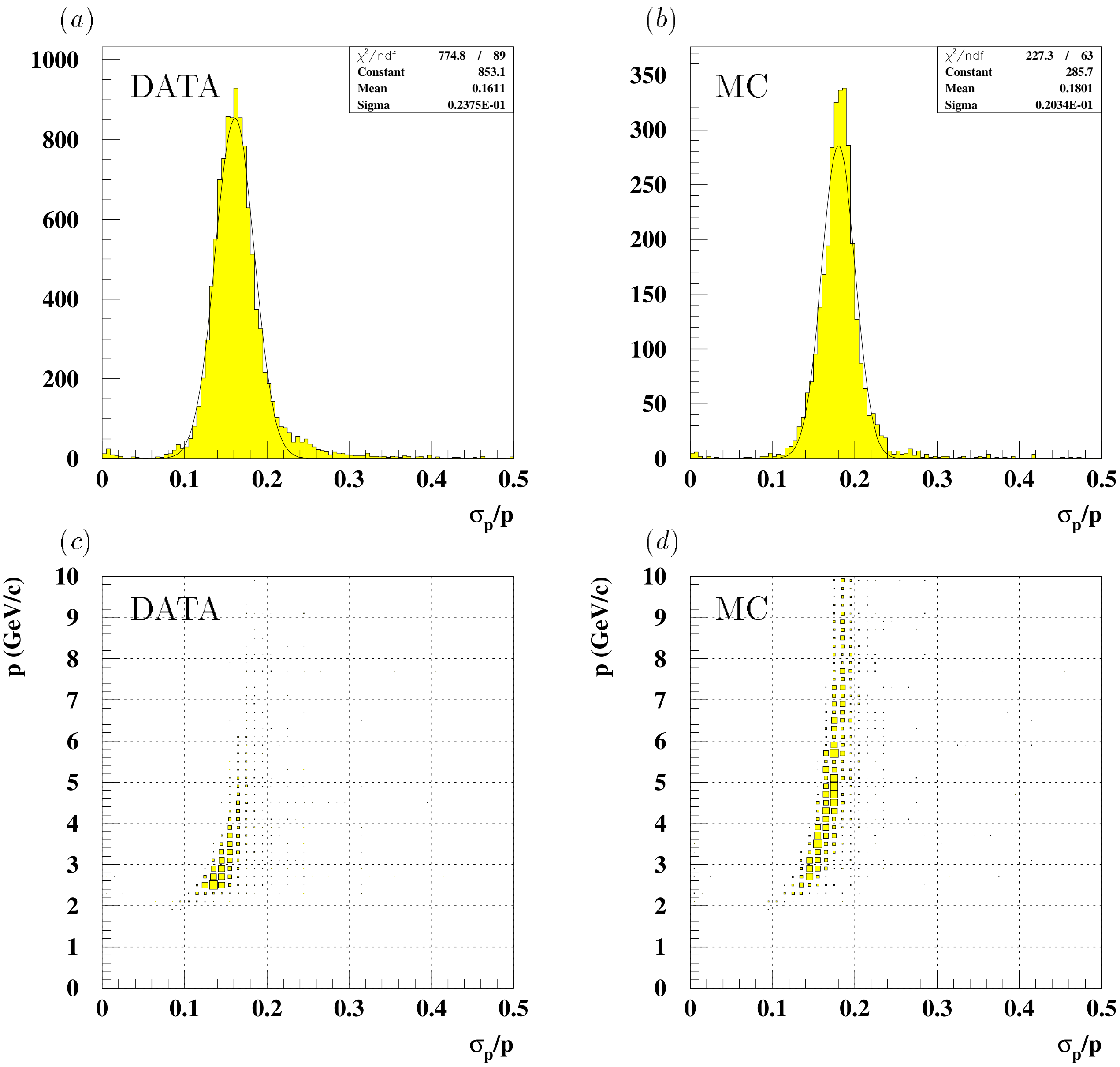

Figure 4.1: The momentum resolution of the FMD. The distribution of σ_p/p is shown for (a) data and (b) Monte Carlo. Plots (c) and (d) show the same distribution for data and Monte Carlo respectively but as a function of the FMD track momentum.

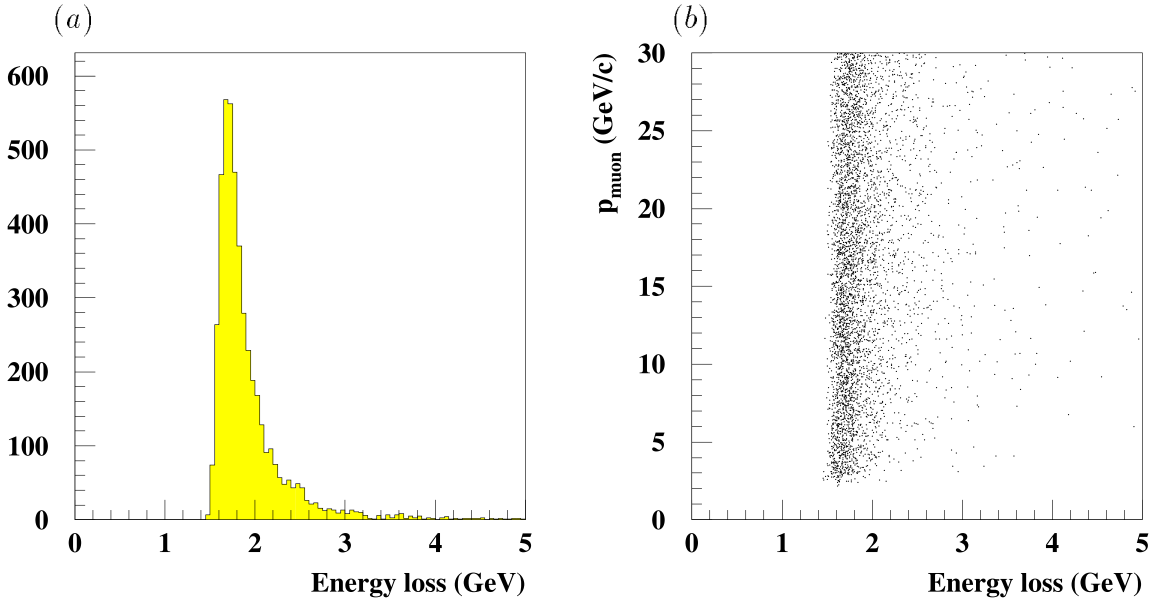

Figure 4.2: (*a*) The energy loss of a muon passing through the toroid and (*b*) the energy loss versus the muon momentum measured in the FMD.

the toroid as a function of muon momentum. Muons entering the FMD with a momentum value of less than 2.25 GeV/c cannot be reconstructed and hence a muon track can only be detected in the FMD if it has an initial track momentum at the vertex of approximately greater than 5.25 GeV/c.

4.3.3 Momentum Correlation Studies

In this section the correlation between the momentum measured by the FTD ($p_{forward}$) and the momentum measured by the FMD (p_{muon}) for a muon track is studied.

Figure 4.3 shows correlation plots for data ((*a*) and (*b*)) and single muon Monte Carlo((*c*) and (*d*)). Plots (*a*) and (*c*) represent the method of hypothesis removal using the link probability selection and plots (*b*) and (*d*) using the FTD transverse momentum. If correlated the links should fall along the diagonal line that has been drawn in each plot. It should be noted that the diagonal line has been drawn to take into account the energy loss of approximately 3 GeV due to the muon going from the vertex to the FMD. In both cases a correlation can be see between $p_{forward}$

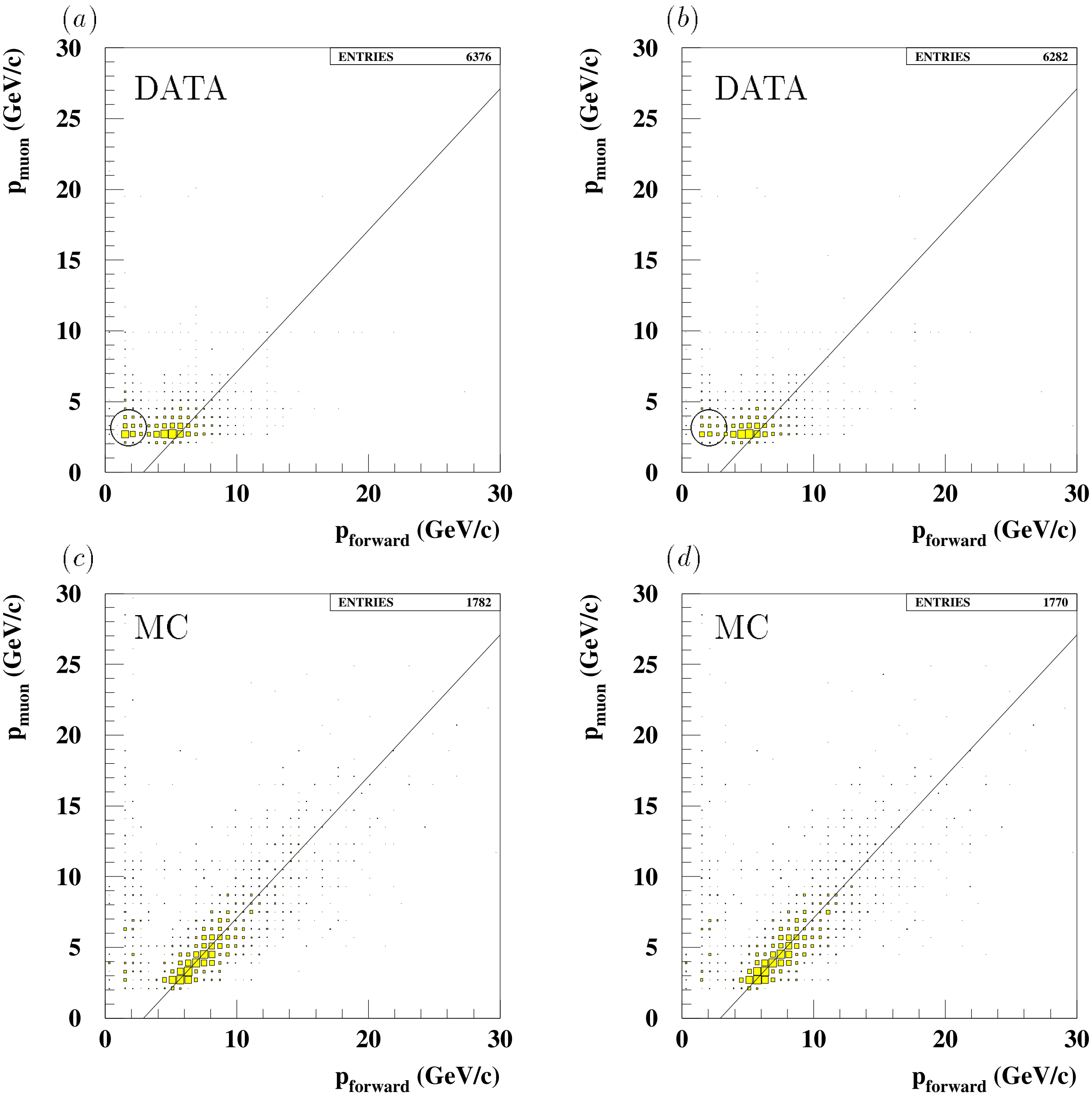

Figure 4.3: FMD track momentum (p_{muon}) plotted against the FTD track momentum ($p_{forward}$). Plots (*a*) and (*c*) represent the method of hypothesis removal using the probability selection and plots (*b*) and (*d*) using the transverse momentum.

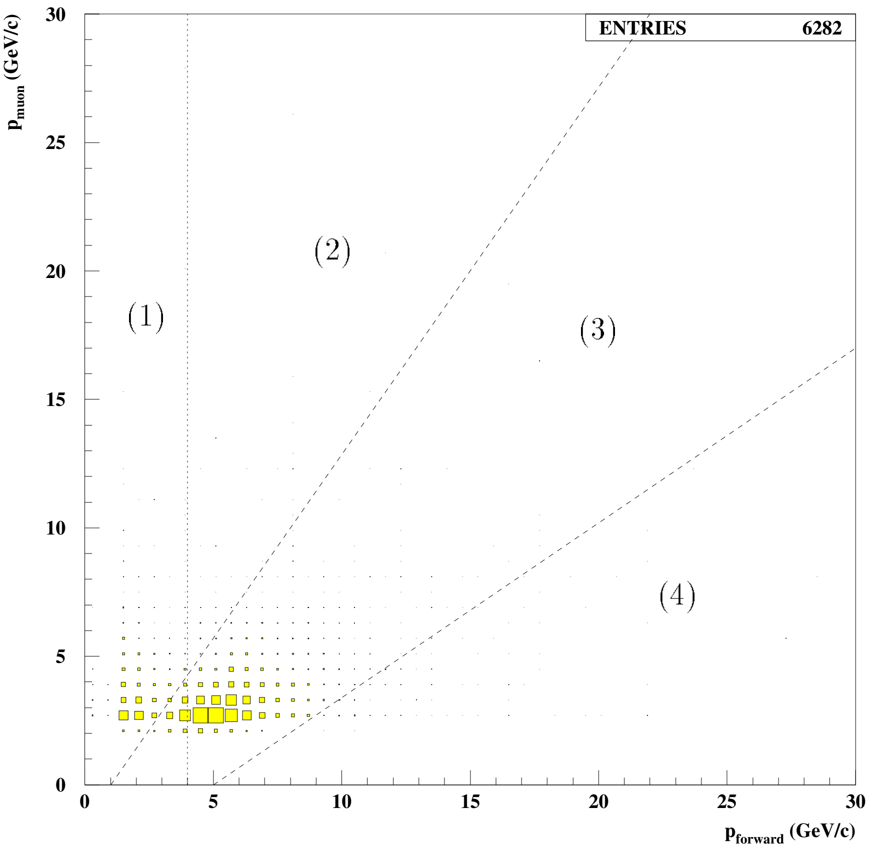

Figure 4.4: Plot of the FMD track momentum (p_{muon}) against FTD track momentum ($p_{forward}$) showing the four study regions.

and p_{muon}.

For data, a population of links lie in the region that has been circled in figure 4.3 (a) and (b). These links suggest that tracks with $p_{forward} < 4\,\mathrm{GeV/c}$ have been detected by the FMD. This is physically impossible because of the amount of the energy loss expected (see section 4.3.2).

In figure 4.3 the data plots for each hypothesis removal method give comparable results. This is also true for the equivalent Monte Carlo plots. However, the population of events in which $p_{forward} < 4\,\mathrm{GeV/c}$ seems to be reduced further in the case of the transverse momentum method of hypothesis removal. Therefore, this method will be used in favour of the probability method.

Figure 4.4 shows an example correlation plot for data between the FMD momentum and the FTD momentum. The plot has been divided into four regions which have been studied separately to illustrate the potential problems that are associated with the linking between the FTD, the iron and the FMD.

Region (1)

In this region FMD tracks have been linked to lower momentum FTD tracks. Taking into account the momentum resolutions of the FTD and the FMD the minimum reconstructed momentum value that a FTD track could have, if it is to be detected in the FMD, is approximately 4 GeV/c. Therefore, the links of region (1) are not ideal links between the FTD and the FMD. These links could be attributed to a FTD track with a badly evaluated momentum value or one that was not reconstructed at all due to a lack of hits in the FTD. In the latter case a different, low momentum, FTD track has been linked instead (this can occur as the extrapolation errors are larger for low momentum tracks).

It is also possible that the FMD has over estimated the momentum of the muon track. However, this is unlikely as a FTD track which has a momentum value less than 4 GeV/c and has still managed to traverse the iron would not leave any hits in the post-toroid layers of the FMD. Therefore, the pre-toroid track segment would have to be linked to a post-toroid track segment made purely from noise. This is unlikely because of the lack of activity in the post-toroid chambers. Hence, if the FMD track has a well defined momentum value then it is unlikely that the false linking can be attributed to an incorrect momentum determination by the FMD.

Figure 4.5 shows an example of a badly linked track. A FTD track of (2.14 ± 0.02) GeV/c has been linked to an iron track of (2.14 ± 2.92) GeV/c and the FTD track has been circled. It should be noted that hits cannot be observed since the tracks have been reconstructed from DST data which do not store hit information. The iron track has, in turn, been linked to a FMD track of (2.76 ± 0.39) GeV/c. A FTD track of (2.14 ± 0.02) GeV/c will not able to reach the FMD so this track must have been incorrectly linked to the iron track. This event suggests that the momentum of the FTD track was under estimated as the θ and ϕ of the track appear to correlate in each detector.

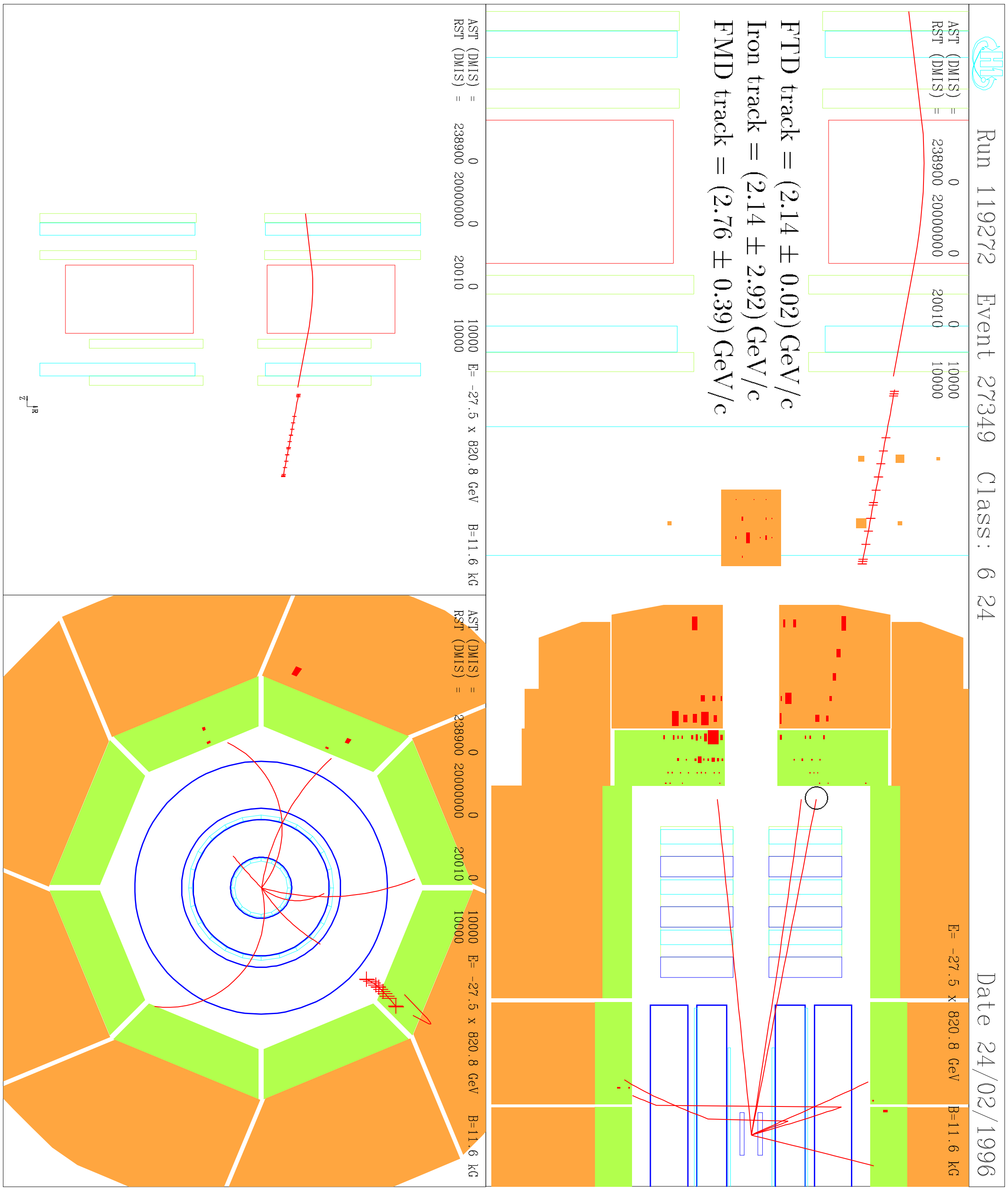

Figure 4.5: An example event for region (1) illustrating a low momentum FTD track that has been linked incorrectly to an iron track.

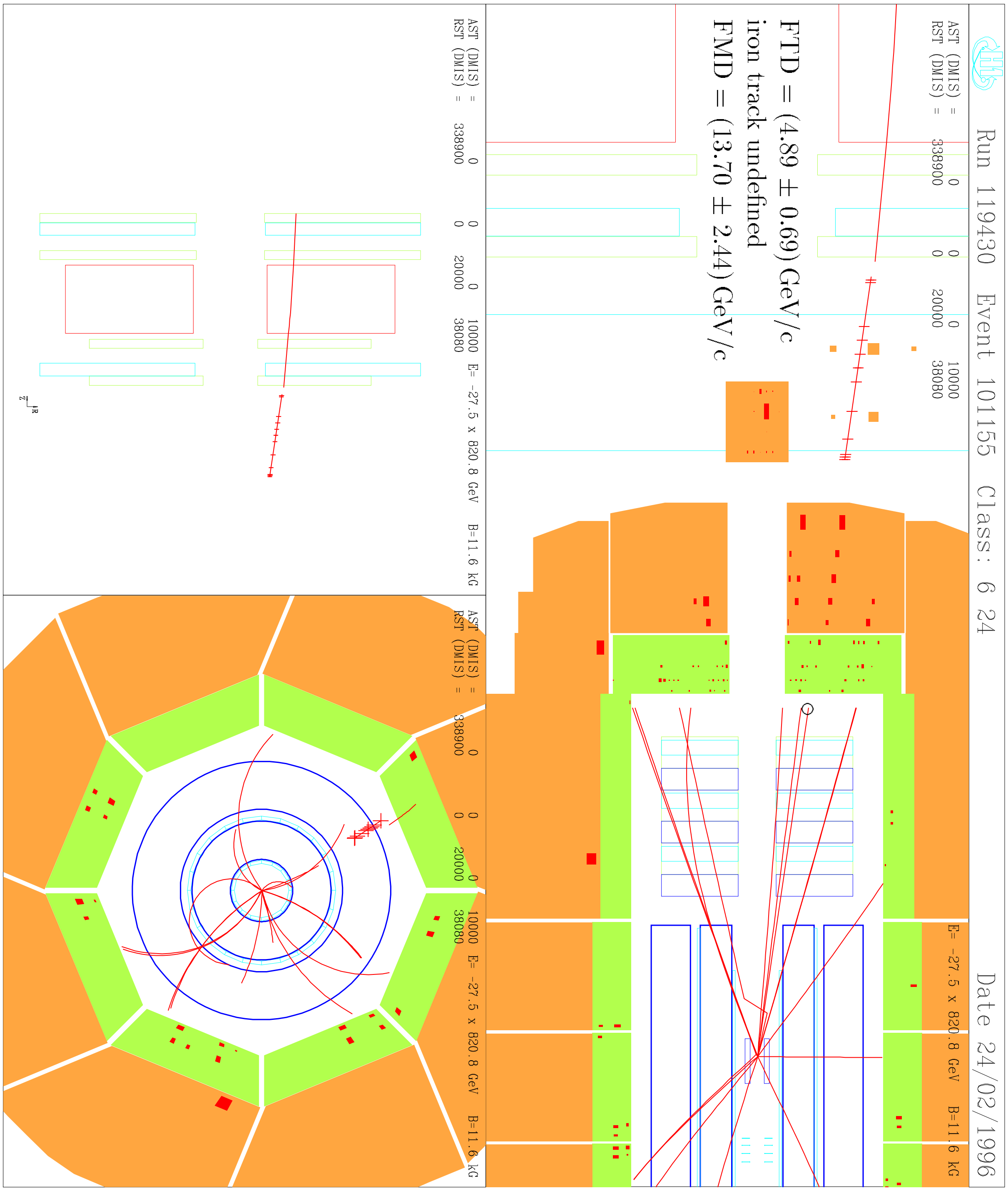

Figure 4.6: An example event for region (2) illustrating incorrect linking due to either the FMD overestimating the track momentum or the FTD underestimating it.

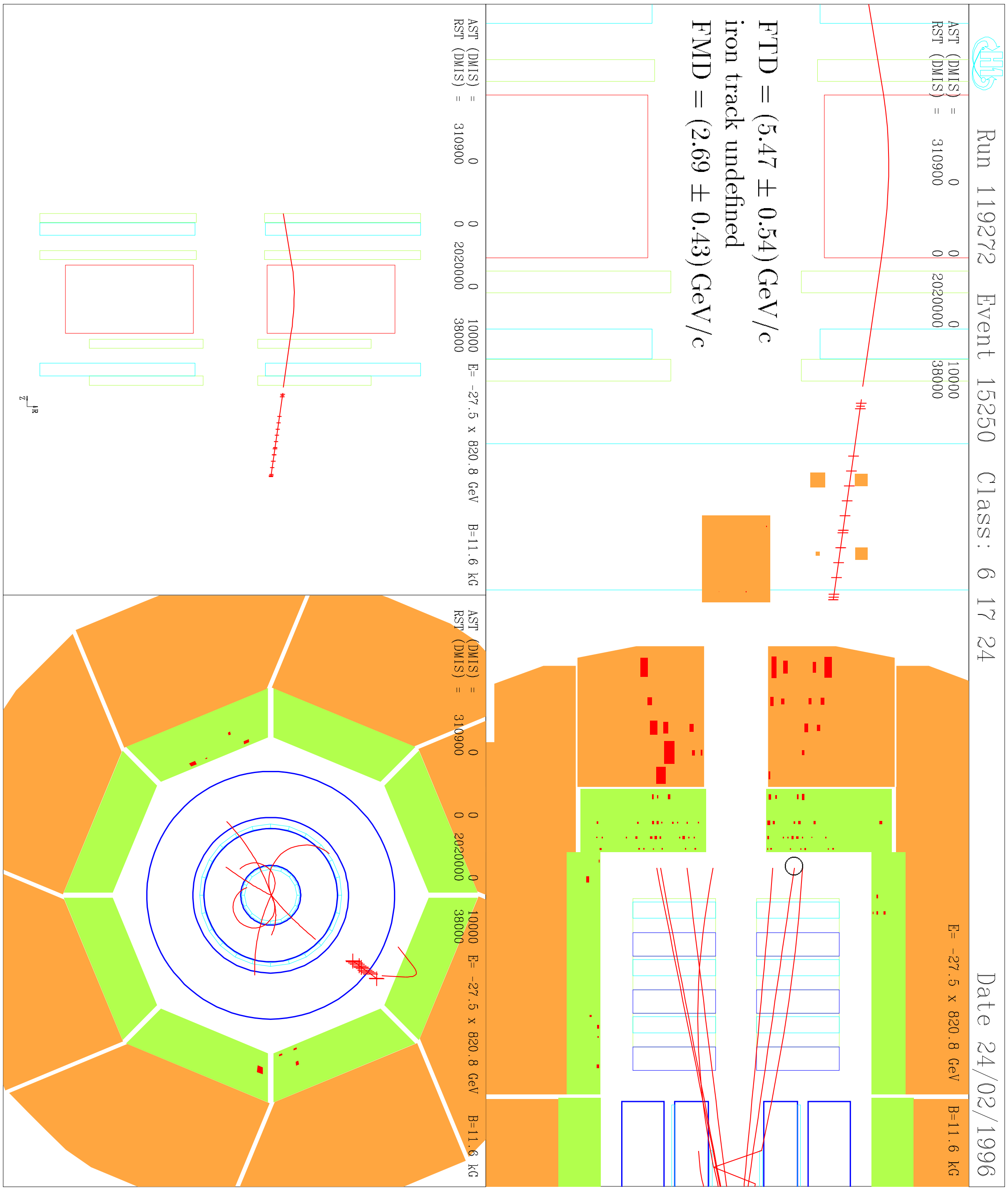

Figure 4.7: An example event for region (3) illustrating a correct linking in which p_{forward} and p_{muon} are correlated when energy losses are taken into account.

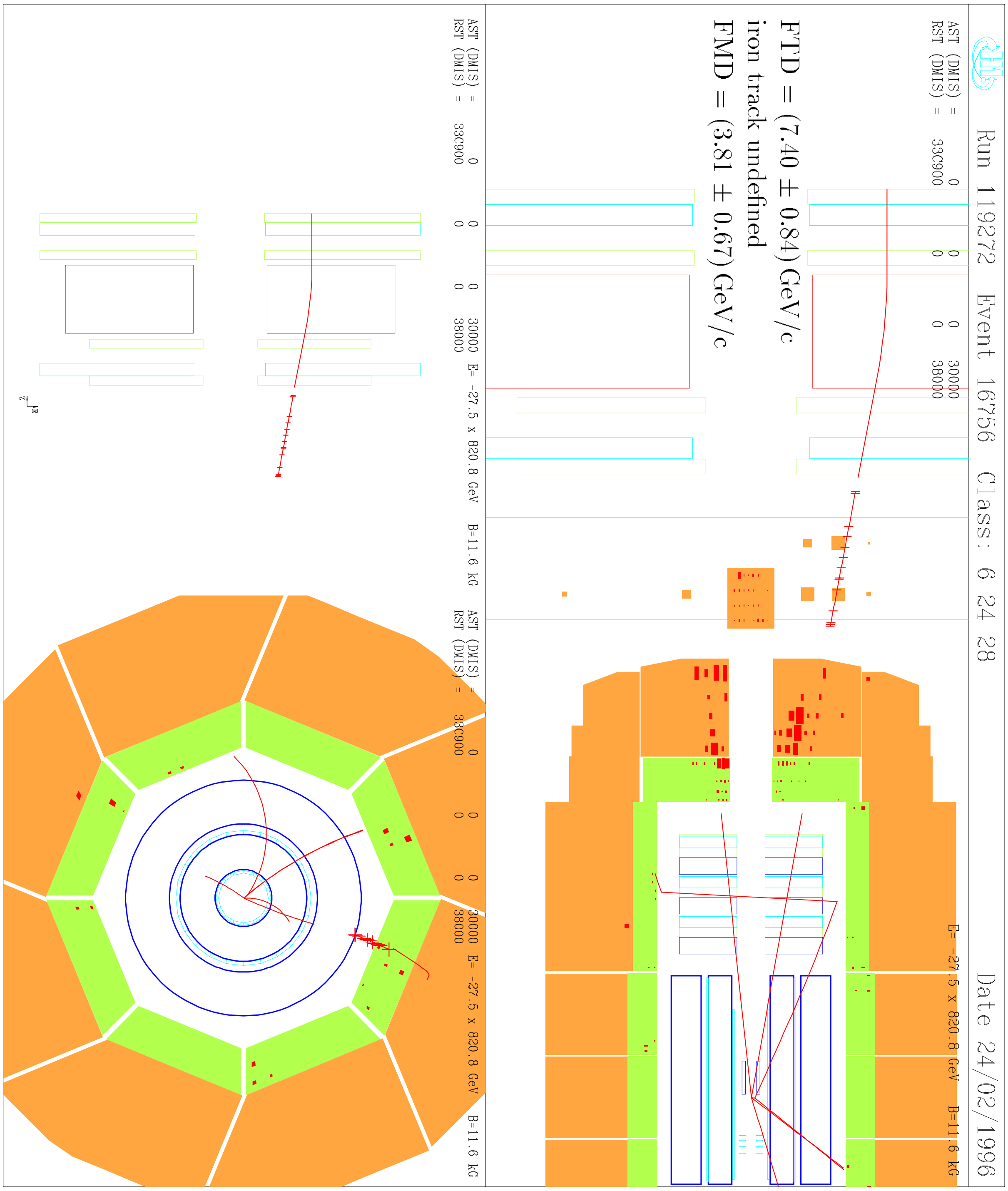

Figure 4.8: An example event for region (3) illustrating a correct linking in which p_{forward} and p_{muon} are correlated when energy losses are taken into account.

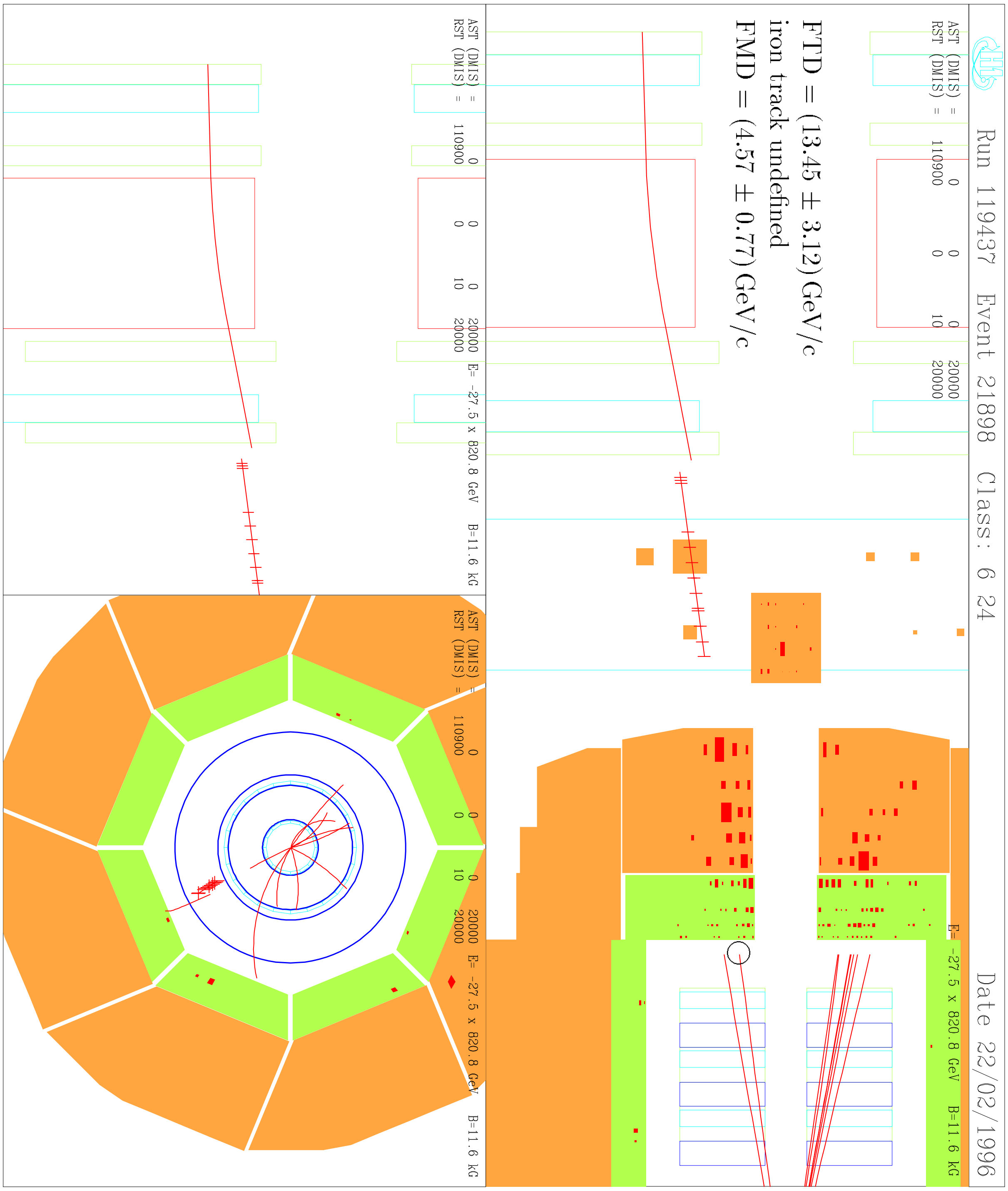

Figure 4.9: An example event for region (4) illustrating an event in which the FMD has under estimated p_{muon} resulting in an incorrect link.

Region (2)

The FTD tracks in this region are linked to higher momentum tracks in the FMD. These events could be examples of incorrect linking or they may be due to the forward tracker under estimating the track momentum of the muon (such as in region (1)). Alternatively the FMD may be over estimating the muon momentum although this is unlikely as the FMD has more of a tendency to under estimate the momentum of the muon.

Figure 4.6 shows an event from this region. The FTD track that has been linked to an iron track has been circled. In this example the FMD track has a momentum value of (13.70 ± 2.44) GeV/c and this is higher than the FTD track which has a momentum value of (4.89 ± 0.69) GeV/c. The iron track momentum is undefined.

Region (3)

This region has been determined from the single muon Monte Carlo (figure 4.3 (*c*) and (*d*)). Events found in this region correspond to when p_{forward} and p_{muon} correlate well, when taking into account the energy losses due to multiple Coulomb scattering in the intervening material.

Two example events in this region are shown in figure 4.7 and figure 4.8. The event shown in figure 4.7 contains a FTD track with a momentum value of (5.47 ± 0.54) GeV/c linked to an iron track with an undefined momentum value which in is turn linked to a FMD track of (2.69 ± 0.43) GeV/c. These momentum values differ by (2.78 ± 0.69) GeV/c which is consistent with the expected energy loss when traveling from the FTD to the FMD.

Figure 4.8 shows an event with a FTD track of (7.40 ± 0.84) GeV/c linked to an undefined iron track. The iron track is linked to a FMD track of (3.81 ± 0.67) GeV/c. These momentum values are again consistent with expected results (differing by (3.59 ± 1.07) GeV/c) and shows that the tracks observed in this region has been correctly linked.

Region (4)

The FTD tracks in this region have momentum values of $p_{\text{forward}} > 5\,\text{GeV/c}$ and are linked to FMD tracks which have lower momentum values. Again, this may be attributed to incorrect linking or it may be due to the forward tracker over estimating the track momentum value or the FMD under estimating the muon momentum value.

An example event where the FMD has under estimated the muon momentum is shown in figure 4.9. The FTD track has a momentum of 13.5 GeV/c which is considerably higher than the FMD track which has a momentum value of 4.6 GeV/c. It can be seen that the FMD pre-toroid track segment is incorrectly determined as it does not appear to compare well with the iron track.

4.3.4 Forward tracker and forward muon hit dependence

Low momentum FTD tracks have larger errors associated with the linking procedure to the muon detectors and so it is more likely that a false link can occur. Therefore, it can be predicted that the number of incorrect links in an event will be proportional to the population of low momentum tracks.

The correlation plot of p_{muon} versus p_{forward} for data is shown as a function of forward tracker planar hits and forward tracker tracks in figure 4.10 and figure 4.11 respectively. Only results for the transverse momentum method for removing hypotheses has been shown (the probability method gives comparable results).

Comparing figure 4.10 (a) and figure 4.11 (a) it is seen that low multiplicity events containing a maximum of 500 planar hits or a maximum of 8 forward tracks have a lower proportion of events in region (1). This shows that the number of false links in this region is correlated with the number of low momentum tracks or equivalently hit multiplicity in the FTD.

This can be visualised in an alternative way when the ratio of the number of links with a FTD momentum value of less than 4 GeV/c divided by the total number of links in the sample is plotted as a function of the number of hits in the planar drift

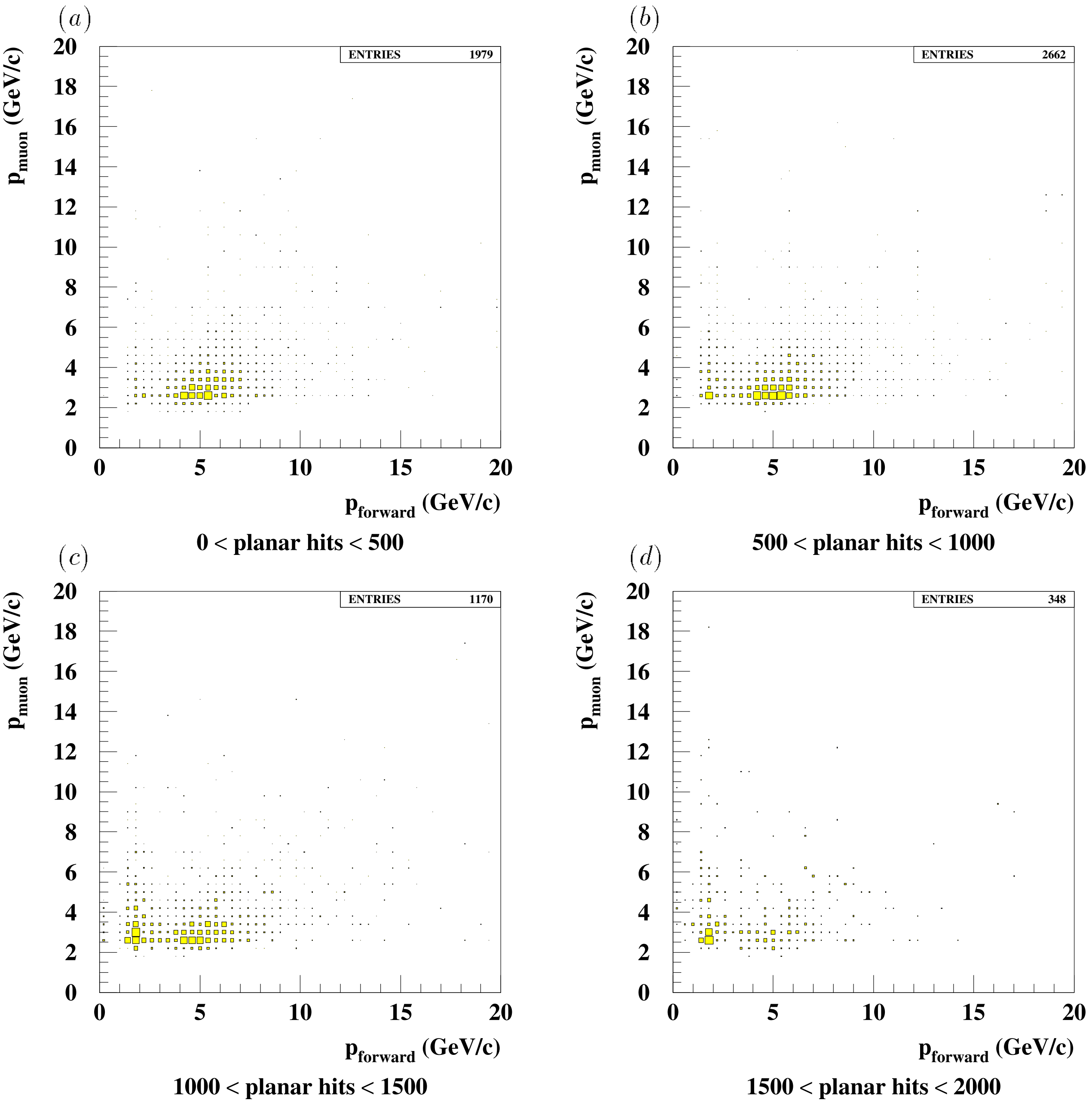

Figure 4.10: FMD track momentum (p_{muon}) plotted against FTD track momentum ($p_{forward}$) as a function of planar hits.

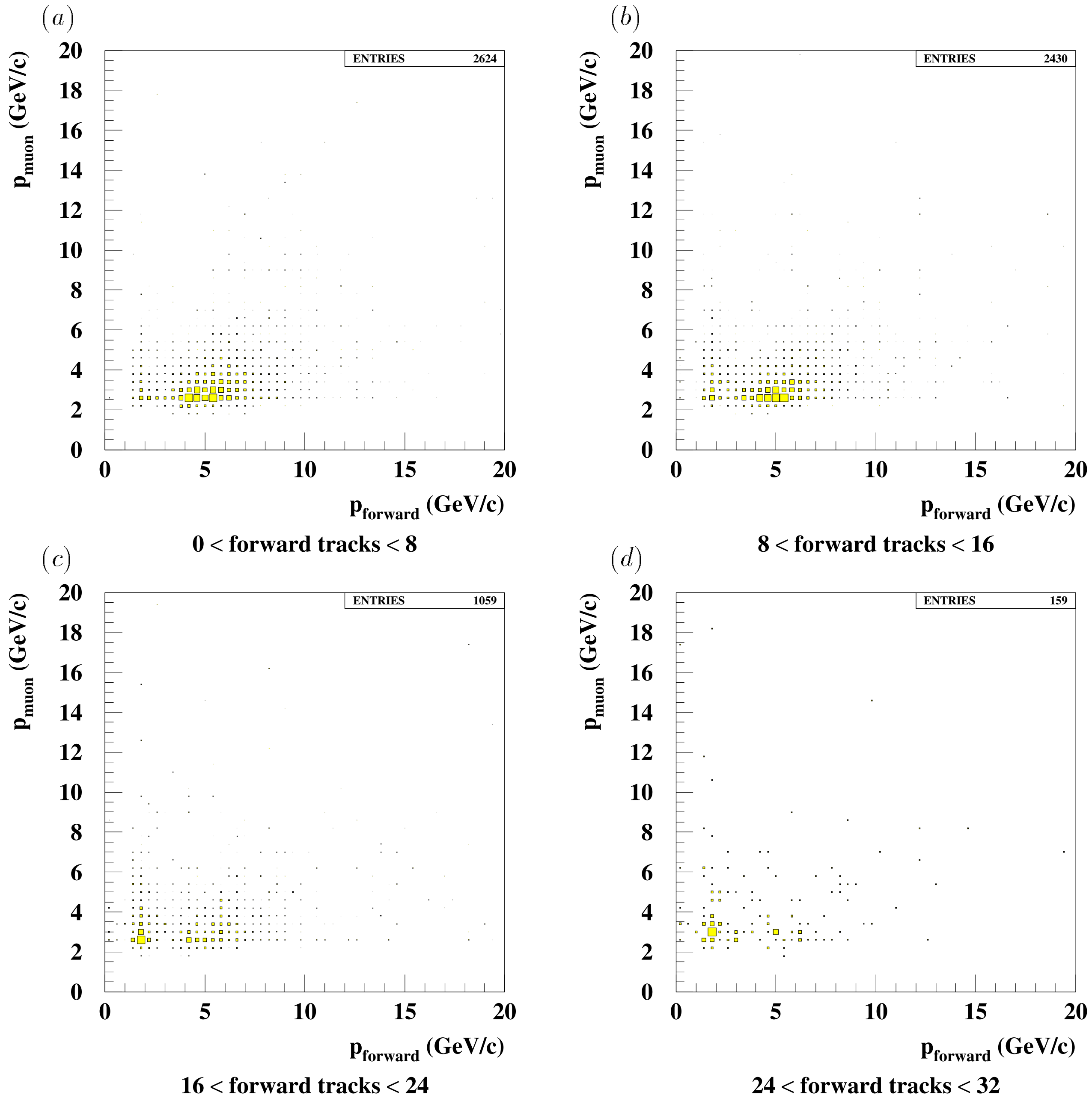

Figure 4.11: FMD track momentum (p_{muon}) plotted against FTD track momentum (p_{forward}) as a function of forward tracks.

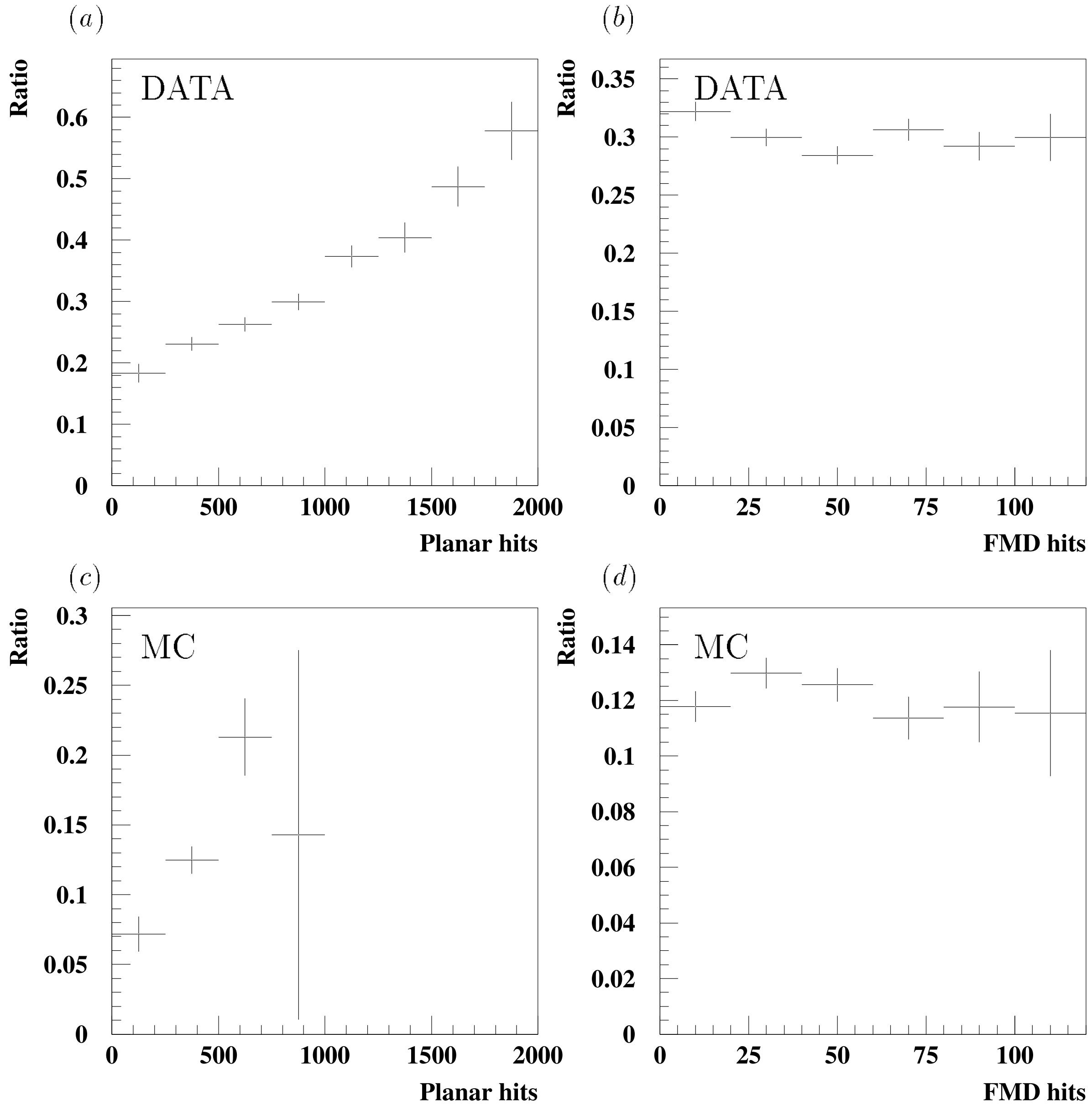

Figure 4.12: Ratio of the number of links with $p_{\text{forward}} < 4$ GeV/c divided by the total number of links in the data sample plotted as (a) a function of the number of hits in the planar drift chambers of the FTD and (b) the number of hits in the pre-toroid layers of the FMD. Plots (c) and (d) are the same plots as (a) and (b) but using the $\chi \longrightarrow J/\psi + \gamma$ Monte Carlo.

chambers of the FTD. Figure 4.12 (a) shows the ratio for data and (c) shows the same ratio for the $\chi \longrightarrow J/\psi + \gamma$ Monte Carlo.

A similar ratio is also plotted in figure 4.12 but as a function of the sum of the number of hits in the θ_1, ϕ_1 and θ_2 chambers of the FMD. Hence a comparison can be made between the number of potential false links made in the FMD and the FTD. Figure 4.12 (b) shows the ratio for data and (d) shows the same ratio for the $\chi \longrightarrow J/\psi + \gamma$ Monte Carlo.

The false link ratio increases by a factor of three when the number of hits detected in the FTD planar chambers increases from 0 to 2000. This suggests that the number of low momentum FTD tracks is dependant on the multiplicity of the event. The increased production of low momentum tracks increases the chance of an incorrect link as low momentum tracks have to undergo the largest deviations due to multiple Coulomb scattering. Hence, at high multiplicites incorrect links can be mainly attributed to the FTD.

The ratio as a function of FMD hits displays a different behaviour with it being approximately constant over the range of 0 to 100 hits detected in the first three pre-toroid layers. The chance of reconstructing a false FMD track is therefore not dependant on the multiplicity of the event and it is likely that the tracks that are detected are valid tracks.

4.3.5 Momentum Residual (Δp)

The momentum residual is defined by the expression:

$$\Delta p = \frac{p_1 - p_2}{\sqrt{\sigma_1^2 + \sigma_2^2}} \tag{4.2}$$

where p_1 and p_2 represent the momentum measurements from the different detectors and σ_1 and σ_2 the errors on p_1 and p_2 respectively. If the momentum values correlate and the errors are correctly estimated the plot of Δp takes the form of a Gaussian of width one, centered at zero.

The values of Δp between the FMD and the FTD for the data and $\chi \longrightarrow J/\psi + \gamma$ Monte Carlo are plotted in figures 4.13 and 4.14 respectively. The plots

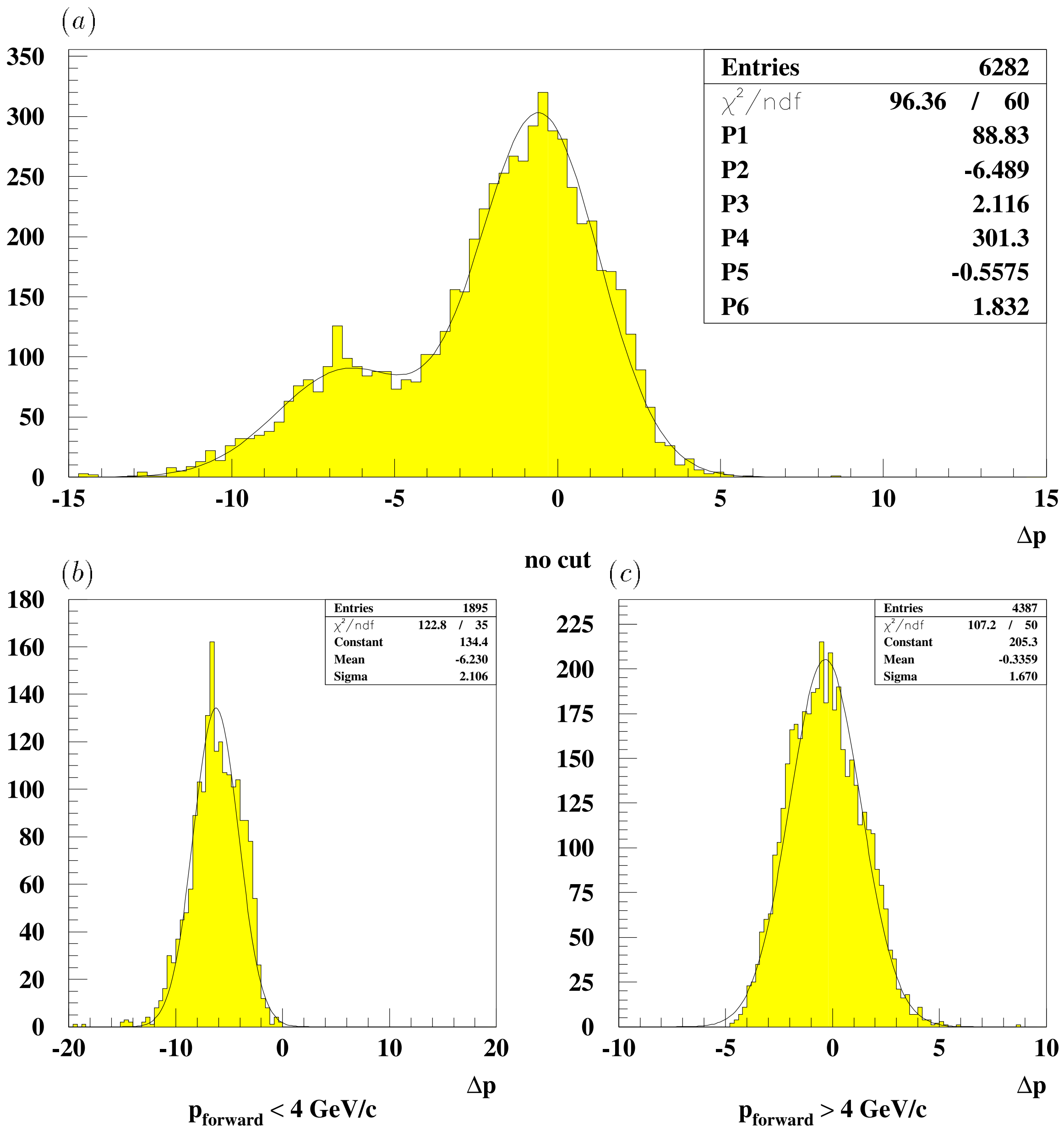

Figure 4.13: Δp calculated using the FTD and FMD momentum values for data with: (a) no cuts, (b) $\mathrm{p_{forward}} > 4\,\mathrm{GeV/c}$ and (c) $\mathrm{p_{forward}} < 4\,\mathrm{GeV/c}$.

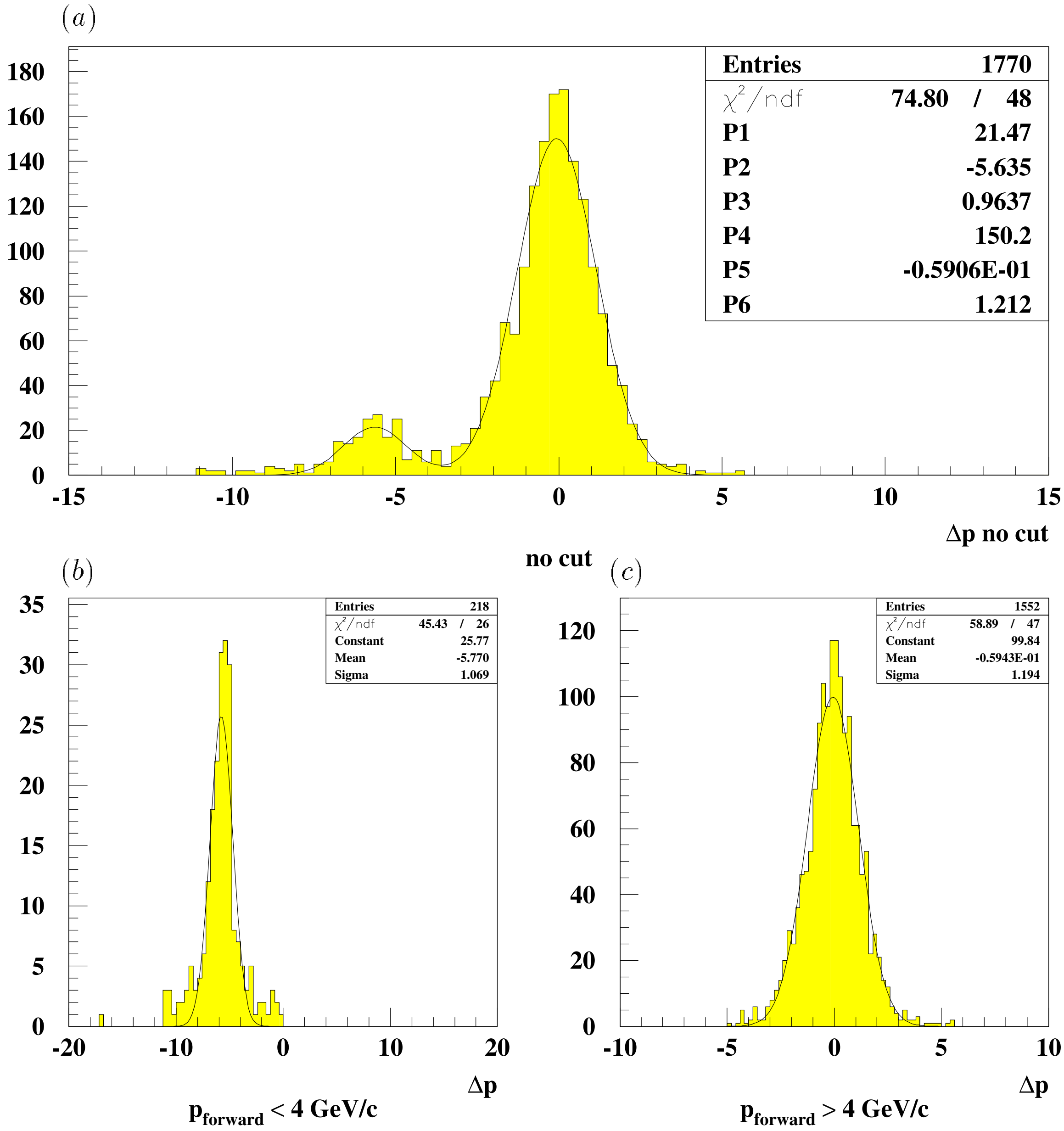

Figure 4.14: Δp calculated using the FTD and FMD momentum values for the $\chi \longrightarrow J/\psi + \gamma$ Monte Carlo with: (a) no cuts, (b) $p_{\mathrm{forward}} > 4\,\mathrm{GeV/c}$ and (c) $p_{\mathrm{forward}} < 4\,\mathrm{GeV/c}$.

represent: (a) Δp before cuts, (b) Δp for $\mathrm{p_{forward}} < 4\,\mathrm{GeV/c}$ and (c) Δp for $\mathrm{p_{forward}}$ $> 4\,\mathrm{GeV/c}$. The plots are fitted with Gaussian functions. Plot (a) for both Monte Carlo and data show a characteristic 'shoulder' which has been fitted separately. The parameters determined from the double Gaussian fit can be compared to the Gaussian parameters given in plot (b) and (c) of figures 4.13 and 4.14. P1, P2 and P3 of plot (a) should be compared to the constant, mean and sigma value of plot (b) and P4, P5, and P6 should be compared to the constant, mean and sigma value of plot (c).

The parameters determined from plot (a) by a double Gaussian fit are compatible with those determined independently by the Gaussian fits to (b) and (c). Hence, the 'shoulder' of plot (a) for both data and Monte Carlo can be explained by the population of links which are in the region (1). However, the population of events in region (1) is greater for data and therefore causes a more pronounced effect to the distribution in figure 4.13 (a).

If the links of region (1) links are ignored, the Δp distribution for data is given by figure 4.13 (c). Comparing the width and mean of this distribution with the same plot for Monte Carlo it can be seen that there is reasonable agreement.

4.4 Summary and Conclusions

The correlation between the FTD momentum and the FMD momentum has been studied for linked tracks and an anomaly has been observed in the region where $\mathrm{p_{forward}} < 4\,\mathrm{GeV/c}$. Due to energy loss and multiple Coulomb scattering is not physically possible that FTD tracks can be linked to FMD tracks in this region. Therefore, incorrect links can be attributed to badly reconstructed FTD tracks. The number of false links for this momentum region is also seen to increase with both the track and hit multiplicity which supports this hypothesis. However, the FMD appears to be working correctly.

Chapter 5

Forward Muon Trigger Efficiency and Acceptance

In this chapter further analysis is carried out on the detection of muons in the forward direction. This detection involves using the Forward Muon Trigger (FMT) to signal the presence of a muon candidate in the FMD.

5.1 The Philosophy of the FMT

The aim of the FMT is to trigger events so that they may be selectively read out. These events must contain tracks detected in the FMD and which point back to the interaction vertex. The pointing requirement is imposed for pre-toroid track segments and also for post-toroid tracks which have transversed the toroid. The pre-toroidal tracks have undergone multiple Coulomb scattering whilst passing through the LAr calorimeter and iron end-cap and the post-toroid tracks have undergone further such scattering in the toroidal iron. Hence, the accuracy at which the track points back to the vertex is degraded (more so for post-toroid tracks).

The inputs to the trigger come from the drift chambers in the θ layers of the FMD which have a 6 cm drift space corresponding to a maximum drift time of $1.2\,\mu$s. As described in Chapter 3, these cells have a staggered configuration (figure 3.2) making it possible to extract the time at which a particle traversed the chambers to better than one HERA bunch-crossing period of 96 ns.

Particles which have penetrated the iron end-cap and have entered the FMD will mainly be muons which are characteristic of heavy-quark production interactions. However, some of these particles may not originate from the electron-proton collisions and constitute background processes which must be rejected. Typical sources of background events have been outlined in Chapter 2. The requirement that a track must point back to the nominal interaction vertex removes a substantial fraction of such tracks.

The logical steps taken by the FMT are shown in figure 5.1. A brief overview of these steps will be given here but a more detailed account can be found in [20]. The trigger finds tracks that hit the same octant and not tracks which cross from one octant to another. The input information to the trigger comes from the linked drift cells. These signals pass through three distinct modules during their processing by the FMT:

- the Discriminator Module;
- the Road Finder Module;
- the Final Decision Module.

These modules are indicated by the shaded areas in figure 5.1.

5.1.1 The Discriminator Module (DM)

The DM detects hits due to charged tracks in the chain of analogue pulses that are sent from the drift cells. Hits are found by determining whether the pulse height rises above a programmable threshold value. These pulses are then digitised and synchronised to the internal H1 clock. Since the cells are coupled by a linking resistor of 330Ω it is also necessary to identify which of the two linked cells was actually struck. This is done by a comparator which samples the amplitude of the pulses on the two wires and allocates the hit to the wire which has the bigger amplitude. After identifying a hit the discriminator is effectively disabled until the next bunch

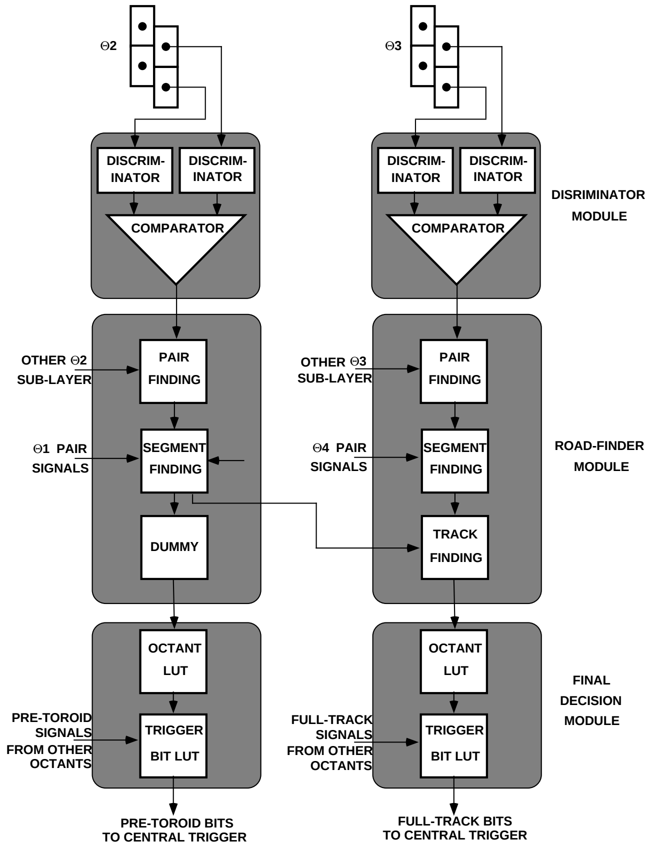

Figure 5.1: Block diagram of the FMT.

crossing so as to avoid double strobing from messy pulses. The final output of the DM's are 48 ns digital signals which correspond to hits. These provide input for the RFM's.

5.1.2 The Road Finder Module (RFM)

These modules have three main tasks:

1. the extraction of t-zero for pairs of wire signals;
2. track finding in θ_1 and θ_2 or θ_3 and θ_4;
3. correlating tracks pre- and post-toroid.

The t-zero value for each pair of cells is extracted by field programmable Application Specific Integrated Circuits (ASIC's) which are known as the *t-zero* chips.

These chips look for pairs of hits (assuming that they point to the H1 vertex) and determine the position of the pair and the event bunch crossing that they originated from. The output from this gives the drift coordinate for the pair of signals, with a resolution of 2 mm.

After pairs of hits have been found, the next stage is to identify and associate pre- and post-toroid track segments. Again this is done by using a set of field programmable ASIC's known as the *track finding* chips (4 chips per RFM). The segment finding procedure can be configured so as to make the requirement that there are either at least three out of four hits per track segment or four out of four hits per track segment. The output from the track finding chips is in the form of a 32 bit map of each octant which describes the position of the track in the drift chamber plane θ_2 for pre-toroid and in θ_3 for post-toroid tracks. This output then forms the input into a set of ASIC's known as the *correlator* chips.

The correlator chips matches pre- and post-toroid track segments to find full validated tracks. They can also introduce a momentum cut by correlating only pre- and post toroid track segments which, when traversing the toroid, have a track bending angle within a programmable pre set value.

The output from the correlator chips in the RFM is essentially information (r and ϕ coordinates) about the positions of the validated tracks in the θ_2 layer of the FMD. The outputs to the FDM are the validated tracks as found by the correlators and the pre-toroid information retained from the track finding stage.

This output is in the form of two 8×8 $r\phi$ bit maps as shown in figure 5.2, one corresponding to pre-toroid tracks and one corresponding to validated tracks. The boxed regions represent one bit and each octant is separated into 8 bits.

5.1.3 The Final Decision Module (FDM)

The FDM processes the two 8×8 $r\phi$ bit maps according to the multiplicities and topologies of the tracks found in the FMD. The output consists of 4 bits each for pre-toroid and full tracks referred to as trigger elements. These eight trigger elements are then sent to the central trigger.

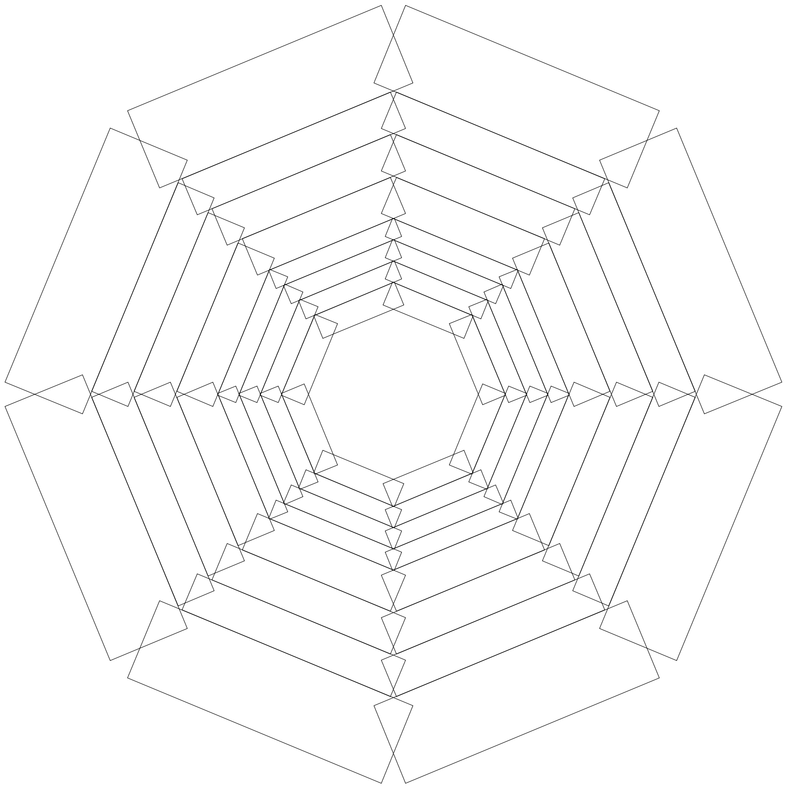

Figure 5.2: An 8×8 $r\phi$ bit map of a θ layer of the FMD.

At present the four trigger elements that correspond to full validated tracks are defined as shown in table 5.1.

5.2 Efficiency and Acceptance

In the following analysis only the efficiency and acceptance of the simplest validated trigger element, 0, is considered. The efficiency and acceptance of the FMT can be determined by studying a sample of events which contain single muons detected in the FMD. These muons must be linked, 'good' quality muons which have been triggered by different subtriggers so that the sample is independent of the FMT.

Figure 5.3 plots (a) and (b) show the momentum and angular distribution of tracks in the FMD. The data sample that is used is described in Chapter 4, section 4.1. The angle that is plotted is the polar angle, θ, for the track point of entry

TRIGGER ELEMENT	DEFINITION
0	Any single muon validated tracks (pre- and post-toroid).
1	A dimuon pair found in opposite octants.
2	More than one validated track found in the same octant.
3	More than one validated track found in different octants.

Table 5.1: The four trigger elements corresponding to validated full tracks.

as oppose to the angle of the track measured by the FMD. It should also be noted that the momentum, p, is that which is measured in the FMD and hence is approximately 3 GeV/c less than the momentum value measured at the vertex. The hashed distribution in each of these plots is a subset of the unhashed distribution and represents events which were triggered by the FMT (trigger element 0). The ratio of these plots is shown in figure 5.3 (c) and (d) and gives the efficiency of the FMT as a function of p and θ. These efficiency plots (c) and (d) are used to determine the angular acceptance and the momentum acceptance of the FMT.

Figure 5.3 (c) shows that the FMT efficiency falls off at approximately 4 GeV/c. This can be explained as a result of the correlator chip which introduces a momentum cut on the bending angle of the track accepted by the correlator. This cut requires that $p_{vertex} > 7$ GeV/c (where p_{vertex} is the momentum value measured at the vertex) which is larger than the minimal reconstructable momentum in the FMD ($p_{vertex} \approx$ 5 GeV/c). This is done so that the requirement of only three hits out of a possible four for a track segment can be used while still maintaining an acceptable trigger rate. This result matches the result determined from Monte Carlo studies [21].

Figure 5.3 (d) shows a lower angle cut off of approximately 8° which is due to

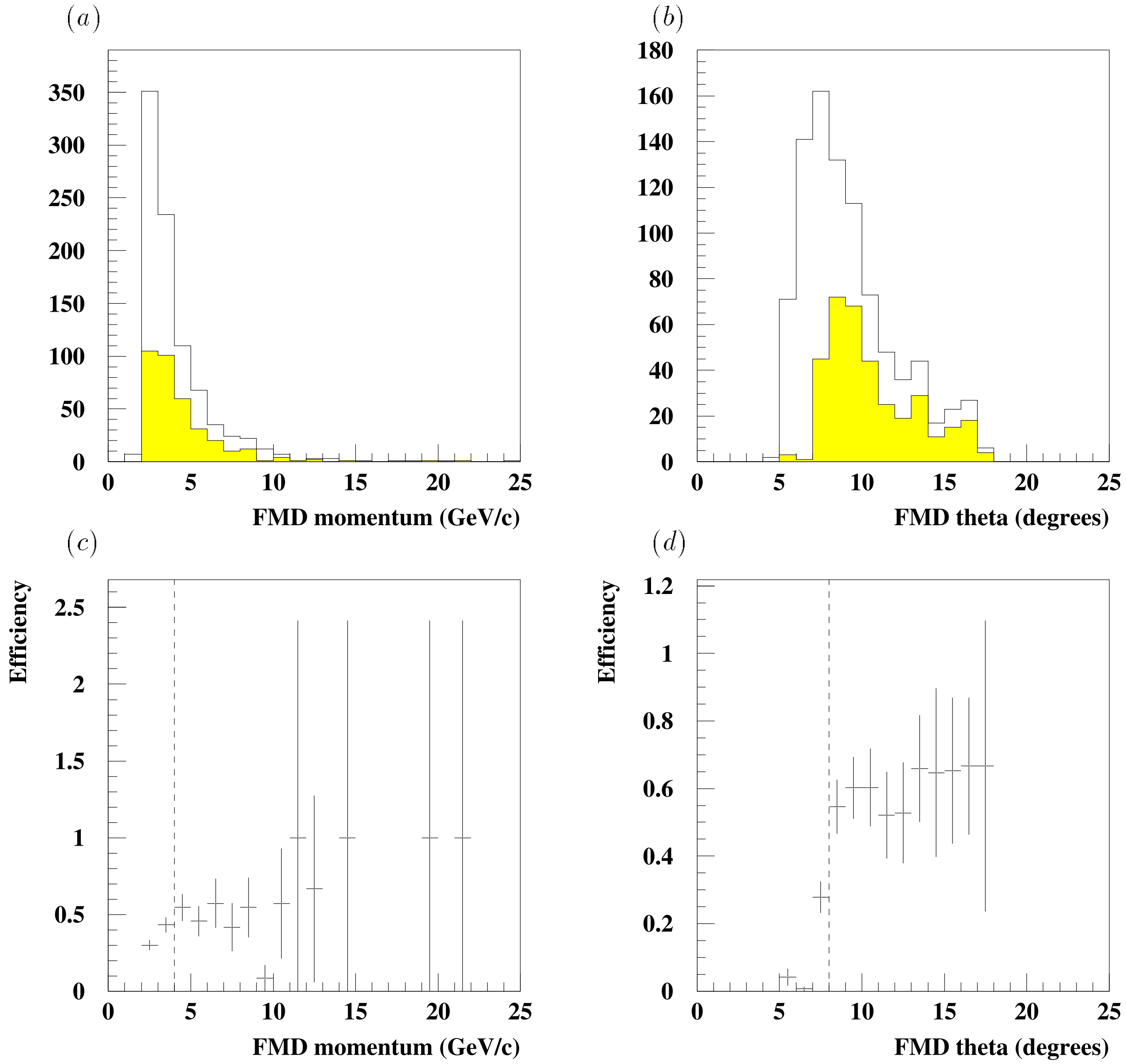

Figure 5.3: Plots (a) and (b) represent the momentum and angular distributions of single muon tracks that have been triggered independently of the FMT and the subset of these distributions in which the events were also triggered by the FMT (hashed). Plots (c) and (d) show the ratio of these two distributions which represents the efficiency of the FMT. From these plots the angular and momentum acceptance of the FMT can be determined.

the fact that the inner region is used to produce a veto for diffractive physics.

Considering only events which are found in the region of good acceptance, defined by $p > 4\,\mathrm{GeV/c}$ and $\theta > 8^\circ$ (indicated by the dashed lines in the plots (c) and (d)) the efficiency of the FMT is calculated to be 83% $\pm$ 3%. The largest contribution is likely to be a result of the single hit finding inefficiencies of the DM, however, a further study is required to understand this value.

Bibliography

[1] F.Abe et al., Phys.Rev.Lett. **74** (1995) 2626.

[2] S.Abachi et al., Phys.Rev.Lett. **74** (1995) 2632.

[3] B.R.Martin and G.Shaw, *Particle Physics*, John Wiley & Sons Inc. (1992).

[4] F.Halzen and A.Martin, *Quarks and Leptons: An Introductory Course in Modern Particle Physics*, John Wiley & Sons Inc. (1984).

[5] J.D.Bjorken, Phys. Rev. **163** (1967) 1767.

[6] J.J.Sakurai, Ann. Phys. **11** (1960) 1;
M.Gell-Mann and F.Zachariasen, Phys. Rev. **124** (1961) 953.

[7] G.Wolf and P.Soding, in *Eletromagnetic Interactions of Hadrons*;
Vol.2,p.1; Eds. Donnachie and Shaw, 1978.

[8] C.F.Weizacker, Z. Phys. **88** (1934) 612;
E.J.Williams, Phys. Rev. **45** (1934) 729.

[9] H1 collab., I.Abt et al., 'The H1 detector at HERA', DESY 93-103 (1993), to be submitted to Nucl. Instr. and Meth.

[10] J.Burger et al., Nucl Instr. and Meth. **A279** (1989) 217.

[11] B. Andrieu et al., Nucl. Instr. and Meth. **A336** (1993) 460.

[12] H1 collab., I.Abt et al., it The H1 detector at HERA, DESY 95-103 (1993), to be submitted to Nucl. Instr. and Meth.

[13] H1 collab., T. Nicholls et al., DESY 95-165 (1995)

[14] H1 collab., R.-D Appuhn et al., DESY 96-013 (1996)

[15] I.Kenyon et al., *The Forward Muon Spectrometer*, DESY 93-020 (1993).

[16] S.Burke et al., RAL-95-037/DESY-95-132, March 1995.

[17] L.West, internal note, *How to use the Reconstruction Code MTREC* (1994).

[18] C.Niebuhr, Private Communication.

[19] L.West, internal note, *How to use the Track Selection Code* (1996).

[20] T.Ahmed et al., RAL-94-126, January 1995.

[21] J.P.Sutton, Private Communication.

Acknowledgements

I would like to thank everyone who has helped me (and put up with me) during the writing of this midterm report. I would particularly like to thank the H1 UK team for providing an entertaining and interesting atmosphere.

I would like to thank Dr I.Kenyon for his advice and also feel special thanks should go to Dr L.West and Dr J.P.Sutton for their patience and endless help.

Extra special thanks and love goes to my fiancé, Mike, who has certainly been the main reason for my survival. His support, along with my parents', can only be said to be irreplacable.

Finally,...thanks Rach for keeping me sober!!!!